Atmospheric turbulence observed during a fuel-bed-scale low intensity surface fire

Joseph Seitz [1], Shiyuan Zhong [1*], Joseph J. Charney [2], Warren E. Heilman [2,*], Kenneth L. Clark [3], Xindi Bian [2], Nicholas S. Skowronski [4], Michael R. Gallagher [3], Matthew Patterson [4], Jason Cole [5], Mike T. Kiefer [1], Rory Hadden [6], and Eric Mueller [6]

[1] Department of Geography, Environment and Spatial Sciences, Michigan State University, East Lansing, MI 48824; seitzjos@msu.edu (J.S.); mtkiefer@msu.edu (M.K.); zhongs@msu.edu (S.Z.)

[2] USDA Forest Service, Northern Research Station, 3101 Discovery Dr., Suite F, Lansing, MI 48910; joseph.j.charney@usda.gov (J.J.C.); warren.heilman@usda.gov (W.H.); xindi.bian@usda.gov (X.B.)

[3] USDA Forest Service, Northern Research Station, Silas Little Experimental Forest, 501 Four Mile Road, New Lisbon, NJ 08064; kenneth.clark@usda.gov (K.C.); michael.r.gallagher@usda.gov (M.G.)

[4] USDA Forest Service, Northern Research Station, 180 Canfield Street, Morgantown, WV 26505; nicholas.s.skowronski@usda.gov (N.S.); matthew.m.patterson@usda.gov (M.P.)

[5] USDA Forest Service, Northern Research Station, 5 Moon Library, 1 Forestry Dr., Syracuse NY 13210; jason.cole2@usda.gov (J.C.)

[6] The University of Edinburgh, Edinburgh, EH9, 3FB, UK; e.mueller@ed.ac.uk (E.M.); r.hadden@ed.ac.uk (R.H.)

* Correspondence to: Shiyuan Zhong, zhongs@msu.edu; Tel.: +1-517-432-4743

1   **Abstract.** The ambient atmospheric environment affects the growth and spread of wildland fires,

2   whereas heat and moisture release from the fires and the reduction of the surface drag in the

3   burned areas can significantly alter local atmospheric conditions. Observational studies on fire-

4   atmosphere interactions have used instrumented towers to collect data during prescribed fires,

5   but a few towers in an operational scale burn plot (usually $> 10^3$ m^2) have made it extremely

6   challenging to capture the myriad of factors controlling fire-atmosphere interactions, many of

7   which exhibit strong spatial variability. Here, we present analyses of atmospheric turbulence data

8   collected using a 4×4 array of fast-response sonic anemometers during a fire experiment on a 10

9   m × 10 m burn plot. In addition to confirming some of the previous findings on atmospheric

10   turbulence associated with low-intensity surface fires, our results revealed substantial

11   heterogeneity in turbulent intensity and heat and momentum fluxes just above the combustion

12   zone. Despite the small plot (100 m^2), fire-induced atmospheric turbulence exhibited strong

13   dependence on the downwind distance from the initial line fire and the relative position specific

14   to the fire front as the surface fire spread through the burn plot. This result highlights the

15   necessity for coupled atmosphere-fire behavior models to have 1-2 m grid spacing to resolve

16   heterogeneities in fire-atmosphere interactions that operate on spatiotemporal scales relevant to

17   atmospheric turbulence. The findings here have important implications for modeling smoke

18   dispersion, as atmospheric dispersion characteristics in the vicinity of a wildland fire are directly

19   affected by fire-induced turbulence.

20

21

1 Introduction

22

23   Wildland fires are directly affected by atmospheric conditions. Macroscale (thousands of

24 kilometers, weeks to months) atmospheric conditions such as prolonged periods without

25 substantial precipitation, high temperature, and low humidity that dry out and pre-heat fuels

26 often set background for large wildland fires (Potter, 1996; 2012; Finney *et al.*, 2015; Littell *et*

27 *al.*, 2016; Kitzberger *et al.*, 2017). Once ignited, fire behavior characteristics (e.g., burn intensity,

28 ember production, spotting, fire whirls and the rate of spread) are influenced more by microscale

29 (< 1000 m, < 1 h) conditions such as local topography and wind speed and direction at the

30 location of the fires. Most wildland fires tend to spread in the direction the wind blows, and the

31 stronger the wind speed the faster the fire spreads (Carrier *et al.*, 1991; Wolff *et al.,* 1991; Clark

32 *et al.,* 1996). Another essential microscale factor affecting fire behavior is atmospheric

33 turbulence, defined as irregular microscale air motions in the forms of eddies that are

34 superimposed on mean atmospheric motions (Stull, 1988).

35   Turbulent eddies affect fire behavior as well as the transfer of gaseous and particulate

36 emissions from the fires to the surrounding atmosphere (Clements *et al.*, 2008; Seto *et al.*, 2014;

37 Viegas and Neto, 2015; Skowonski and Hom, 2015; Heilman *et al.*, 2015; Heilman, 2021).

38 Turbulence in the atmosphere is generated primarily by wind shear as a result of changes in wind

39 speed and/or direction, known as mechanical turbulence, and by convection, referred to as

40 thermal turbulence. Mechanical turbulence is often generated when air flow encounters surface

41 drag, rough terrain or other natural or man-made obstacles and boundaries separating different

42 air masses (e.g., weather fronts), different land cover types (e.g., grass vs. forested land) or land

43 use types (e.g., agriculture vs. urban). Thermal turbulence is produced when heated surface air

44 rises up in the atmosphere, a process known as convection, which commonly occurs during

45   daytime when incoming solar radiation absorbed by the earth's surface exceeds outgoing

46   terrestrial radiation. Fire-induced turbulence is a type of thermal turbulence in that heat released

47   by combustion produces buoyant plumes that rise up from the combustion zone.

48   Despite the important role atmospheric turbulence plays in fire behavior and in the

49   exchanges of momentum and scalars (e.g., heat, moisture, carbon monoxide, carbon dioxide

50   particulate matter or PM) between the combustion zone and the surrounding atmosphere,

51   detailed observations of atmosphere turbulence in the presence of wildland fires have only

52   become available in recent decades. For instance, the first large-scale field experiment where

53   comprehensive turbulence data were collected above and in the vicinity of a wildland fire front

54   was FireFlux, conducted on February 23, 2006 over a 40-hectare plot of native tall-grass prairie

55   in Galveston, Texas (Clements *et al.,* 2007; Clements *et al.,* 2008). Fire-atmosphere interactions

56   were monitored primarily using fast-response three-dimensional (3D) sonic anemometers

57   mounted at multiple levels on a tall (43 m) and a short (10 m) tower within the burn plot. The

58   data revealed a fivefold increase in turbulence kinetic energy and a threefold increase in surface

59   stress during the fire-front passage, and a rapid return of turbulence to the ambient level behind

60   the fire front. A follow-up field experiment, known as FireFlux-II, took place at the same site in

61   2013, with more measurements designed to fill gaps in the original FireFlux experiment and

62   provide further information on fire–atmosphere interactions and fire-induced turbulence regimes

63   (Clements *et al.,* 2019). The data from FireFlux II have been used to validate fire behavior

64   models (Moody *et al.*, 2022), but the results on the intensive collection of turbulence data from

65   FireFlux II are yet to be reported in the peer-reviewed literature.

66   While the FireFlux and FireFlux II experiments in Texas provided direct turbulence

67   measurements during intense grass fires, a number of wildland fire experiments in the New

Jersey Pine Barrens provided information on fire-induced turbulence during low-intensity forest

understory fires (Heilman *et al.* 2015, 2017, 2019 and 2021; Mueller *et al.* 2017, 2019; Clark *et*

al. 2020). These experiments were conducted between 2010 and 2021 by research projects under

the auspices of the Joint Fire Science Program (http://www.firescience.gov) and the Department

of Defense Strategic Environmental Research and Development Program (SERDP)

(https://serdp-estcp.org/). The burn plots for these experiments, which were in the same areas of

the New Jersey Pine Barrens, ranged from about 5 to 100 hectares in size, with forest understory

vegetation (average about 1 m height) composed of blueberry, huckleberry and scrub oak and

overstory vegetation (average about 20 m height) composed of pitch pine and mixed oak.

Turbulence data were collected using 3D sonic anemometers and thermocouples mounted on a

20-m, a 10-m and a 3-m micrometeorological flux tower within the burn plots. The data from

these NJ fire experiments revealed large variations in turbulence intensity, stress, and fluxes

across the canopy layer, which complicated the evolution of local turbulence regimes and their

interaction with the spreading fires. Specifically, the data showed that fire-induced increases in

turbulent kinetic energy are considerably larger near the top of the forest canopy layer than

within the canopy, implying that vertical mixing or transport of fire emissions (e.g., PM,

moisture and heat) could be substantially larger near the canopy top than within the canopy layer

(Heilman *et al.,* 2015). The observations also revealed that an anisotropic turbulence regime

tends to persist throughout the vertical extent of overstory canopy layers, even within the highly

buoyant plume during the passage of fire fronts. The results suggested that spreading line fires

can have a substantial effect on the skewness of daytime velocity distributions typically found

inside forest vegetation layers, and that the contributions to turbulence production and evolution

90   from mechanical shear production and diffusion can be very different in the pre-fire and post-fire

91   environments (Heilman *et al.,* 2017).

92   The data from both the TX grass fires and NJ forest understory fires have also provided

93   insight into the turbulent momentum and heat transfer processes during the fires. The fire-

94   enhanced turbulence updrafts and downdrafts transfer warmer air (or lower momentum air) from

95   the surface upward, a process known as "ejection" and colder air (or higher momentum air)

96   downward to the surface, a process referred to as "sweep", which act to redistribute energy or

97   momentum between the combustion layer and the atmosphere above (Heilman *et al.*, 2021). The

98   analyses of the data from the TX and NJ fire experiments suggested that wildland fires in grass

99   or forest environments could substantially alter the relative importance of sweep and ejection

100   processes in redistributing momentum, heat and other scalars in the lower atmosphere (Heilman

101   *et al.,* 2021). For turbulent momentum transfer, sweep events were found to play a dominant role

102   at the fire front regardless of fire type despite the stronger updrafts than downdrafts at the front.

103   However, the effect of fires on turbulent heat transfer is different between the heading intense

104   grass fires and backing low-intensity forest-understory fires. The former tends to be dominated

105   by ejection events while in the latter case ejection and sweep events are equally important

106   (Heilman *et al.,* 2021).

107   Both the TX and NJ fire experiments mentioned above were conducted over plots on

108   relatively flat terrain. However, wildland fire behaviors can be affected significantly by

109   topography (Werth *et al.,* 2011; Sharples, 2009; Sharples *et al.,* 2012). This is because

110   topography exerts a strong influence on both weather and fuel conditions (Bennie *et al.*, 2008;

111   Ebel, 2013; Billmire *et al.*, 2014; Calviño-Cancela *et al.,* 2017; Povak *et al.*, 2018). A series of

112   prescribed burn experiments in California between 2008 and 2012 were conducted in complex

113 terrain with burn plots on a simple slope (Seto and Clements *et al.,* 2011; Seto *et al.*, 2013;

114 Clements and Seto, 2015; Amaya and Clements, 2020) or in a narrow valley (Seto and Clements,

115 2011). The burn plots in these experiments ranged from 2 to 15 hectares in size, but all plots

116 were dominated by grass fuels. Data from these experiments collected using

117 micrometeorological towers augmented by other remote sensing equipment provided unique

118 information on the interactions between terrain-induced circulations and fire-induced flows. The

119 results showed that terrain-induced slope flows and valley winds can interact with fire-induced

120 flows to enhance horizontal and vertical wind shears that subsequently contribute to turbulence

121 production. The interactions of fire-induced flows with slope winds also produce local

122 convergence or divergence with strong updrafts and downdrafts. Turbulence regimes tend to be

123 anisotropic immediately above fire fronts, moving towards isotropic conditions higher up (Seto

124 *et al.,* 2013, Clements and Seto, 2015; Amaya and Clements, 2020). The data from these studies

125 also revealed an increase in turbulent energy in both velocity and temperature spectra at higher

126 frequencies, as fire fronts shed small eddies, and an increase at lower frequencies that are related

127 to the strengths of the cross-stream wind component generated by the fire and enhanced by

128 topography (Seto *et al.*, 2013).

129   The aforementioned field experiments were conducted on operational-scale (or

130 management-scale) burn plots that ranged from several to 100 hectares and it was not feasible to

131 cover such large burn plots with just a few micrometeorological towers. Consequently, the

132 measurement strategy of these experiments was centered around tall towers placed at couple of

133 key spots in the burn plot to provide information on vertical variations of fire-atmosphere

134 interactions. The lack of spatial coverage of the complex fuel and atmospheric conditions at

135 these large burn sites makes interpretation of the limited observations challenging. Laboratory

136 studies (e.g, Forthofer and Goodrick, 2011; Campbell-Lochrine *et al.*, 2021; Di Cristina *et al.*,

137 2022) have the advantage of monitoring the fires using densely spaced instruments. However,

138 laboratory studies are often conducted under controlled conditions not necessarily representative

139 of the real fuel and atmospheric environments encountered in outdoor wildland fires. There

140 exists an apparent gap in the observations of fire-atmosphere interactions between operational-

141 scale burns and fine-scale laboratory experiments.

142   Here, we present analyses of turbulent data collected during a small-scale (10 m ×10 m)

143 experimental burn in the field that was densely instrumented for the purpose of bridging the gap

144 in our knowledge about fire-atmosphere interactions between operational-scale ($\geq 10^3$ m^2) and

145 laboratory-scale ($< 10^1$ m) fire experiments. The primary question we aim to address is how a

146 low-intensity surface fire may modify turbulence in the atmosphere just above the combustion

147 zone. More specifically, our analyses will explore the following questions: How does the surface

148 fire alter turbulence intensity and turbulent heat and momentum exchanges between the

149 combustion zone and the atmosphere above? Whether and how would the fire change the

150 partitioning of the heat and momentum fluxes into different types of events (both event number

151 and event contribution)? How does the modifications of the fire on turbulence vary spatially

152 across the burn plot? Answers to these questions could prove useful for predicting fire-

153 atmosphere interactions, particularly the momentum and scalar exchanges between the fire and

154 the atmosphere. Moreover, the answer to the last question could provide guidance regarding

155 what horizontal grid spacing in coupled atmosphere-fire behavior models is necessary to capture

156 horizontal variability in near-surface atmospheric turbulence during the presence of surface fires.

157

158

2 Method

2.1 Experiment and Instrumentation

The experimental burn that this study focuses on took place on May 20, 2019 in a pitch

and loblolly pine plantation at the Silas Little Experimental Forest in New Lisbon, New Jersey.

This particularly burn was part of broader series of 35, densely instrumented, low-intensity

surface fire experiments on 100 m^2 (10 m x 10 m) plots in this plantation conducted between

March 2018 and June 2019 by a SERDP research project that set out to collect data using

laboratory-scale (10^0-$10^1 m^2$) experiments, intermediate or fuel-bed-scale (10^2 m^2) burns and

management-scale (10^{3-4} m^2) prescribed fires to improve the understanding of combustion

processes and fire-atmosphere interactions across scales (Gallagher *et al.*, 2022; Skwonski, *et al.*,

2021).

As shown in Figure 1, the 100 m^2 burn plot was densely monitored by instruments

mounted on four parallel east-west-oriented trusses (A, B, C, D). On each truss, four 3D fast-

response sonic anemometers (R.M. Young 81000V, Traverse City, MI, USA) were mounted at

2.5 m above the ground level (AGL) to collect the east-west (u), north-south (v) and vertical (w)

velocity components and temperature at a sampling rate of 10 Hz (Clark *et al.*, 2022a).

Additional 10-Hz temperature data were also obtained using fine-wire thermocouples (Omega

SSRTC-GG-K-36, Omega Engineering, Inc., Stamford, CT, USA) mounted at a range of heights

(0, 5, 10, 20, 30, 50, 100 cm) below the two inner trusses (B and C) (Clark *et al.*, 2022b). A

radiometer/visible spectrum camera pair was mounted adjacent to each sonic anemometer to

measure radiative heat fluxes and flame arrival times and persistence (Kremens *et al.*, 2022).

Spatially explicit fire spread data were derived from infrared data collected by an infrared video-

camera (A655SC, FOL6 100.0-650.0 C lens, FLIR Systems Inc., Wilsonville, OR, USA)

183   mounted on top of a 10-m tower in the center of the plot (Skowronski *et al.*, 2022a). A custom

184   field calorimetry hood (labeled TACO next to B2) with an inlet oriented over a portion of the

185   fuel bed was used to sample O_2, CO_2, and CO concentrations in buoyant plumes (Campbell-

186   Lochrie *et al.*, 2022). Gas concentrations were measured at 1 Hz using an Infrared gas analyzer

187   (Crestline NDIR 7911, Crestline, Livermore, CA, USA).

188   The analyses here focused only on the data from the 4×4 sonic anemometer array. All

189   sonic anemometer data underwent a quality assurance and control process to remove spurious

190   values (Clark *et al.*, 2022a). Initially, data that were collected prior to a designated common start

191   time was removed, providing a starting point for the observations for the burn period. Next, the

192   data from sonic anemometers include a self-reporting diagnostic column where any non-zero

193   number is considered an invalid measurement, so any measurement that reported a non-zero

194   diagnostic code was removed. Following these initial steps, data that fell outside the sonic

195   anemometer operating parameters (wind speed: ±40 m/s; temperature: ± 50 °C) were also

196   removed.

197   The horizontal wind velocities were rotated into a streamwise coordinate system where

198   the *u*-component (streamwise component) is aligned with the prevailing wind direction, and the

199   *v*-component (cross-stream component) is perpendicular to the prevailing wind direction pointing

200   to the left. Vertical winds were not corrected for tilt because of the short (<30 min) observational

201   period and because the burn plot was on level ground and each sonic anemometer was carefully

202   mounted and leveled so that the wind sensors were very close to true horizontal and vertical

203   planes. The results (presented below) indeed suggested that the contamination of vertical

204   velocity by horizontal velocities were negligibly small as the average vertical wind component

205   during the pre-burn period was nearly zero.

9

206

2.2 Fuel and ambient atmospheric conditions

208   The primary fuel for this burn was pitch pine needles (*Pinus rigida* Mill.). Based on

209 biometric and terrestrial laser scan measurements collected pre- and post-burn, the fuel mass was

210 estimated to be about 0.5 kg m^{-2} and fuel moisture content about 5.5% (Skowronski *et al.*,

211 2022b).

212   The ambient atmospheric conditions on the day of the burn is indicated using the data

213 from a surface weather station located approximately 200 m northeast of the burn plot that has

214 similar type of land cover as the burn plot (Figure 2). Ambient winds were very weak in the

215 morning, varying in direction between south and west. Wind speeds increased in midday to about

216 5 m s^{-1} along with a direction shift to southwest and west. This wind speed increase was likely

217 due to the mixing of higher winds from above to the surface as the mixing layer grew higher

218 during the day. The growth of the mixing layer was a result of increased turbulent mixing

219 associated with surface heating, as indicated by an increase in surface temperatures from about

220 20 °C in the morning to slightly above 30 °C around 1400 Local Standard Time (LST) and a

221 corresponding decrease in relative humidity from over 80% in the morning to less than 40% in

222 the early afternoon.

223

2.3 Fire spread

225   The experiment started around 14:25 LST when a single 10-meter cotton cord was

226 soaked in accelerant, ignited and then dropped on the fuel bed to produce a single, near linear

227 ignition across the western border of the plot. Infrared imagery data (Figure 3) captured by the

228 overhead infrared camera is used to evaluate the changes in temperature from just before ignition

229   (Figure 3a), immediately after ignition (Figure 3b), and through the period following the ignition

230   as the line fire spread with winds across the plot (Figure 3c-f). The average fire spread rate

231   throughout the burn was evaluated from these data to be approximately 5.4 cm s^{-1}. The ignition

232   produced a line fire parallel to the western boundary of the plot (Figure 3b). The line fire spread

233   in the direction of the west-southwesterly background wind towards the east-northeast over the

234   next few minutes (Figure 3c, d). The initial spread was faster on the northern portion of the

235   domain, as expected from the south-southwesterly wind direction. As the fire burned through the

236   northern portion of the plot, the fire front caught up in the southern portion (Figure 3e). The fire

237   ended at around 14:32:16 LST as the fire front reached the eastern boundary of the plot and ran

238   out of fuel to continue (Figure 3f).

239

240   **2.4 Data Analysis**

241   The quality-controlled 10-Hz wind and temperature data from the 3D sonic anemometers are

242   used to calculate turbulent perturbations defined as the differences between the instantaneous

243   observations and the mean values:

244 $$\varphi' = \varphi - \overline{\varphi} \tag{1}$$

245   where $\overline{\varphi}$ is the mean value that is estimated by block-averages

246
247 $$\overline{\varphi} = \sum_{n=1}^{N} \varphi_n \tag{2}$$

248

249   Here, N is the number of samples over the averaging period or the time block and the mean

250   values represent the mean state of the atmospheric flow. In traditional turbulence studies, mean

251   state is usually determined by averaging the data over a period of a few minutes up to 1 hour,

252   depending on atmospheric stability and the scale of interest. However, the block-averaged values

253   during the period of active burning are likely to be contaminated by the fire and therefore poorly

254   represent the mean background flow. To resolve this issue, Seto *et al.* (2013) and Heilman *et al.*

255   (2015) proposed that the block-averaged means for the fire period be replaced by block-averaged

256   means calculated during the pre-burn period. In order to adopt this approach, the observational

257   period is divided into three periods representing pre-burn, burn and post-burn, which are

258   described in detail below.

259   The arrival of the fire front at most locations in the sonic anemometer array was clearly

260   marked by a sharp rise in temperature (Figure 4). However, the magnitudes of the temperature

261   increase and the rates of increase vary with the location of the sonic anemometers because the

262   shape of the flame front was irregular (Figure 3). Note that the sonic temperatures are limited to

263   50 °C, which is the operational range for the instruments beyond which data are deemed

264   unreliable. Based on the temperature time series and the time when the fire was ignited along the

265   western boundary (14:25 LST), the 10-min period from 14:15:13 through 14:25:12 LST is

266   defined as the pre-burn period over which the mean values for u, v, S (horizon wind speed), w,

267   and T are calculated, and these values are used for computing perturbations for the entire

268   experiment. The definition of the burn period, however, is complicated by the fact that the fire

269   front reaches/leaves each sonic anemometer at a different time and consequently the true burn

270   period across the plot varies somewhat depending on the location of each sonic anemometer.

271   To create a robust definition of the burn period that can be applied to all the sonic

272   anemometers in the 4 × 4 array, and eventually to other burns in the broader burn series, the

273   sharp rise in sonic temperatures associated with fire front is measured using integer (n) multiples

274   of the standard deviation (denoted using σ) of the average temperature over the pre-burn period.

275   A threshold value that is too small (e.g., 1 or 2 times standard deviation) may not distinguish the

276   increase in temperature associated with the fire front from normal temperature fluctuations

277 during the day, but a value that is too large (e.g., 10 time standard deviation) may fail to detect

278 the fire front associated with a small or moderate temperature increase. Figure 5 shows the

279 number of sonic anemometers whose temperatures exceed $n \times \sigma$ as n increases from 1 to 35, and

280 the length of the exceedance period. As n increases from 1 to 8 or the threshold value for fire-

281 induced temperature increase changes from 1σ to 8σ, the number of sonic anemometers drops

282 from 16 to 13 and the period drops sharply from just under 60 min to about 6 min. Continued

283 increases in the threshold values from 8σ to 25σ result in no change in the number of

284 anemometers and very little change in the length of the period (less than 1 min). This analysis

285 suggests that 8σ can be used as the threshold for temperature increases associated with fire front.

286 Thresholds lower than 8σ would imply a burn period of 30- to 60-min long that, according to the

287 time series in Figure 4, would include periods of no fire and therefore de-emphasize the effects

288 of the fire in the resulting analyses. Applying this criterion to all the sonic anemometers and

289 defining the burn period as between the first and last sonic temperature at or above the threshold

290 leads to the selection of the burn period as 14:26:13 to 14:32:29 LST. Finally, the 10 min

291 following the burn period (14:32:30 to 14:42:29 LST) is defined as the post-burn period.

292   Following the establishment of the three periods, wind and temperature perturbations are

293 calculated using equations (1) and (2), where the pre-burn averaged values are used as means for

294 the burn and post-burn periods. Strictly speaking, the perturbations calculated for the burn and

295 post-burn periods are not classical turbulent perturbations; to differentiate the features from

296 classical turbulence, they should be interpreted as being primarily fire-induced turbulent

297 perturbations.

298   As noted above, horizontal wind velocity is rotated into a streamwise coordinate where

299 the x-component (streamwise component, u) is aligned with the prevailing wind direction and the

300   y-component (cross-stream component, v) is perpendicular and pointing to the left of the

301   prevailing wind. The prevailing wind direction for the rotation is determined by the 10-min pre-

302   burn period average of wind directions across all 16 sonic anemometers. The average wind

303   directions during the pre-burn period vary slightly across the 16 sonic anemometers, with mean

304   and median wind directions of 225 and 226 degrees, respectively. The subtle variations in wind

305   directions is possibly due to slight error in sensor alignment, rather than actual flow

306   heterogeneity. The 226 degrees is used as the prevailing wind direction for the purpose of

307   coordinate rotation.

308   The quality controlled, coordinate rotated data from the sonic anemometers are analyzed

309   to determine fire-induced changes to turbulence intensity, vertical heat fluxes and vertical fluxes

310   of horizontal momentum also known as shear stress just above the combustion zone by

311   comparing values between the pre-burn and the burn periods. The values are also compared

312   between the pre-burn and post-burn periods to determine how quickly the effects of fire dissipate

313   or how fast the atmosphere returns to the ambient state.

314   Turbulence intensity is measured by the turbulent kinetic energy (TKE) defined as the

315   sum of the variance of the three velocity components:

316

317
$$TKE = \left(\overline{u'^2} + \overline{v'^2} + \overline{w'^2}\right)/2 \qquad (3)$$

318

319   Turbulent shear stress is commonly measured by shear velocity or friction velocity denoted by

320   u_* and the square of friction velocity is related to the magnitude of the kinematic vertical flux of

321   horizontal momentum:

322
$$u_*^2 = \left(\overline{u'w'}^2 + \overline{v'w'}^2\right)^{\frac{1}{2}} \qquad (4)$$

14

323   where u'w' and v'w' are the vertical fluxes of streamwise and corss-stream momentum flux,

324   respectively and the overbar denotes time average. The average period is 1 min for this analysis

325   to be consistent with previous studies on fire-induced turbulence (Seto *et al.*, 2013; Heilman *et*

326   *al.* 2021). Vertical heat flux is calculated as $\overline{T'w'}$ and the averaging period is also 1 min.

327   For the analyses of vertical turbulent fluxes of heat and horizontal momentum, a quadrant

328   analysis technique (Katul *et al.,* 1997, 2006; Heilman *et al.,* 2021) is utilized to delineate the

329   contributions to the turbulent heat or momentum transfer from four types of processes

330   corresponding to the four quadrants of a *w'*(horizontal) and φ' (vertical) coordinate, where the *w'*

331   denotes vertical velocity perturbation and φ' denotes perturbations of temperature (*T'*) or

332   horizontal wind speed (*S'*) in heat or momentum flux calculations, respectively. The four

333   quadrants are: Q1: $\varphi'w' > 0$, $\varphi' > 0$, $w' > 0$; Q2: $\varphi'w' < 0$, $\varphi' > 0$, $w' < 0$; Q3: $\varphi'w' > 0$, $\varphi' <$

334   0, $w' < 0$; Q4: $\varphi'w' < 0$, $\varphi' < 0$, $w' > 0$. Note that the perturbation in horizontal wind speed

335   (*S'*), rather than the streamwise or cross-wind components (*u'* or *v'*), are used for computing

336   momentum flux following Heilman *et al.*, (2021):

$$S' = S - \overline{S} \qquad (5)$$

$$S = \sqrt{u^2 + v^2} \qquad (6)$$

339   The quadrant analysis is also known as sweep-ejection analysis (Heilman *et al.*, 2021)

340   which associates each quadrant with a specific type of vertical turbulent transfer events. The

341   names of the events and the associated quadrant designations, which are different for turbulent

342   heat and momentum fluxes, are given in Table 1.

343   Based on the definition in Table1, ejection (Q1) and sweep (Q3) events contribute to

344   positive vertical turbulent heat flux through the upward transfer of warmer air from below

345   (ejection) or the downward transfer of cooler air from above (sweep), while inward interaction

346   (Q2) and outward interaction (Q4) events contribute to negative turbulent heat flux through the

347   downward transfer of warmer air from above (inward interaction) or the upward transfer of

348   cooler air from below (outward interaction). For vertical flux of horizontal momentum, inward

349   interaction and outward interaction events contribute to positive flux through the upward transfer

350   of faster moving air (outward interaction) or the downward transfer of slower moving air (inward

351   interaction), while sweep and ejection events contribute to negative momentum flux through the

352   downward transfer of faster moving air (sweep) or the upward transfer of slower moving air

353   (ejection). Note that the warmer/cooler or faster/slower air is relative to the air in the adjacent

354   layers.

355   The sweep-ejection analysis calculates the proportion of a given type of events by simply

356   counting the number of events or the data points in the 10 Hz time series that fall within the

357   given quadrant. The contributions of the given type of events to the average turbulent fluxes over

358   a given time period (T_p) are calculated, following Heilman *et al.* (2021), by the integral

359

360                $$\overline{\varphi'w'}_Q = \frac{1}{T_p}\int_0^{T_p} \varphi'(\tau)w'(\tau)\varepsilon_Q d\tau \qquad\qquad (7)$$

361

362   where ε_Q is 1 for the given quadrant and zero otherwise, τ is time and φ' is temperature or

363   horizontal wind speed perturbation for heat or momentum fluxes, respectively.

364

365   **3 Results and Discussion**

366

367   **3.1 Fire-Induced Perturbations to Wind and Temperature**

368   Before we examine fire-induced changes to turbulence in ambient atmosphere, we first

369   take a look at the response of the instantaneous temperature and wind to the surface line fire

370   recorded by the 16 sonic anemometers as the fire spread from west to east across the 10 m ×10 m

371   burn plot (Figure 6). Note that perturbation temperatures (T', see Eq. 1), instead of actual

372   temperatures, are shown to accommodate the magnitude difference between temperature and

373   wind and therefore making it easier to visualize jointly the effects of the fire on temperature and

374   wind. The natural or non-fire fluctuation recorded during the pre-burn period are small, with

375   magnitudes generally less than 2.5 m s^{-1} for u, 1 m s^{-1} for v and 2.5 °C for T'. The fire impinging

376   upon the sonic anemometers is marked by a sharp increase in T', but the magnitude of the

377   temperature changes depend heavily on location, from very little change on the western side (A1,

378   B1, C1, D1) of the burn plot where the fire was ignited, to a nearly 20°C increase on the eastern

379   side (A4, B4, C4, D4). This spatial heterogeneity in T' is consistent with the pattern of the fire

380   spread from the western boundary toward the east and northeast by the southwesterly ambient

381   wind (Figure 4). During the burn period, the u fluctuations decreased slightly while the v

382   fluctuations increased. The v-component no longer fluctuated around zero, as in the pre-burn

383   period, but rather it was dominated by negative values, indicating a systematic shift in wind

384   direction. There was a tendency for u and T' to return towards the pre-burn conditions after the

385   burn, but the v component remained negative during the post-burn period.

386   The observed changes in the distribution of wind and temperature values associated with

387   the fire at all 16 sonics are summarized by the box-whisker plots in Figure 7. The pre-burn mean

388   is 1.7 m s^{-1} for the streamwise wind component u and near zero (-0.04 m s^{-1}) for the cross-stream

389   component v. The pre-burn vertical velocity distribution also has near zero mean, which

390   confirms that the sonic anemometers were well-leveled. During the burn period, the mean of u

17

391   dropped in magnitude from 1.7 to 1.05 m s^{-1} while the mean of v increased in magnitude from -

392   0.04 to -0.65 m s^{-1}, indicating an overall shift in wind direction from southwesterly to west-

393   southwesterly. This change in the horizontal wind components suggests that ambient air was

394   drawn towards the fire producing convergence at the fire front. There is also a fire-induced

395   widening of the distributions of the horizontal wind components, particularly the v component,

396   and an increase in the number of outliers with magnitudes that nearly doubled the pre-fire

397   magnitude. The large negative values in v during the burn period reinforce the suggestion of

398   convergence in the vicinity of the fire.

399   Interestingly, there is little evident change in the overall distribution of w during the burn

400   period, except that more and larger outliers are indicated. The maximum updrafts (downdrafts)

401   during the burn period reach speeds of nearly 6 m s^{-1} (-5 m s^{-1}), which is more than double those

402   of the pre- and post-burn periods, suggesting that intermittent turbulent eddies associated with

403   the fire could have a strong impact on vertical velocity just above fuel bed. The T' distribution

404   also widens substantially during the burn period (σ=4.24 ℃) compared to the pre-burn period

405   (σ=0.48 ℃), with the maximum temperature perturbation reaching nearly 20°C.

406   The influence of the fire on the horizontal wind components continues into the post-burn

407   period, as the post-burn distributions of u and v fall between those of the pre-burn and burn

408   periods. In contrast, the post-burn w distribution returns to a distribution very close to that of the

409   pre-burn period. Similarly, the T' distribution during the post-burn period is very similar to that

410   of the pre-burn period. The similarities between the w' and T' distributions suggest that the two

411   variables are closely related to each other, with large updrafts during the burn period being

412   generated primarily by heating. This result suggests that the fire-induced circulation exhibits

413   behavior more consistent with a buoyant plume than mechanically forced rising motion resulting

414   from converging surface air.

415

3.2 Intensity of Fire-Induced Turbulence

417   We now explore the modifications of the fire to atmospheric turbulence properties just

418   above the combustion zone. The first question to address is how turbulence intensity quantified

419   by *TKE* in Eq. (3) is modified by the fire and how the modification may vary with location in the

420   burn plot. Figure 8 shows time series of 1-minute averaged *TKE* and its three components (the

421   variance of the three velocity components) for each of the sonic anemometers. The time series

422   indicate lower *TKE* values in the pre-burn period, larger values during the burn period, and

423   values remaining high in the post-burn period. The burn period *TKE* is primarily driven by an

424   increase in horizontal velocity variance, $\overline{u'^2}$ and $\overline{v'^2}$, particularly the cross-stream component

425    $\overline{v'^2}$. The *TKE* values remain high into the post-burn period and, at several sonic anemometers

426   (D3 and C4), the post-burn *TKE* peaks are comparable with or higher than the peaks observed

427   during the burn period.

428   The box-whisker plots in Figure 9 depict the fire-induced changes to the distribution of

429   turbulence intensity as observed by all 16 sonic anemometers. Averaging across all the

430   instruments, the burn period mean *TKE* is 1.25 m^2s^{-2}, which is roughly double the pre-burn mean

431   of 0.697 m^2s^{-2}. The interquartile range of the burn period *TKE* is nearly three times the pre-burn

432   period range. Despite the increase in the mean and the interquartile range of the *TKE* from the

433   pre-burn to the burn period, the mean *TKE* values are still below 3 m^2s^{-2}, which is a threshold

434   sometimes used as an indicator for substantial boundary-layer turbulence (Stull, 1988; Heilman

435   and Bian, 2013), suggesting that this low-intensity surface line fire fails to produce a

19

436   substantially turbulent environment at the levels just above the fuel bed. The mean *TKE* in the

437   post-burn period does not return to that of the pre-burn period and remains elevated (1.21 m^{2}s^{-2}).

438   While the $\overline{w'^2}$ returns to the pre-burn conditions, the horizontal components remain elevated.

439   More specifically, $\overline{u'^2}$ and $\overline{v'^2}$ make up 53.0% and 38.5% of the average pre-burn *TKE*,

440   respectively. During the burn period, the contribution to *TKE* from $\overline{u'^2}$ decreases slightly to

441   49.1% and the contribution from $\overline{v'^2}$ increases substantially to 43.3%. As noted earlier (Figures 6

442   and 7), the burn period also exhibits a larger range of horizontal and vertical wind components,

443   which is consistent with the larger range of *TKE* values in Figure 9.

444   In the post-burn period, the distribution of vertical velocity variance returns to the pre-

445   burn distribution. However, the range of values in the horizontal components are smaller during

446   the post-burn period than the burn period, but still larger than during the pre-burn period. The

447   medians of the horizontal *TKE* components are higher in the post-burn period than in either of

448   the other periods. While the $\overline{u'^2}$ outliers (above the 99.3rd percentile) decrease, the $\overline{v'^2}$ outliers

449   increase in magnitude. As was previously discussed, post-burn average wind directions differ

450   slightly from the pre-burn, accompanied by increases in the magnitude of the horizontal winds

451   (Figures 6 and 7). This result is consistent with elevated *TKE* values persisting into the period

452   after the end of the fire.

453   Additional analysis of the variance of the three velocity components enables an

454   assessment of turbulence anisotropy indicated by the ratio of $\overline{w'^2}$ to 2x*TKE*. When this ratio

455   approaches 1/3 for a given time period, the period can be said to experience an isotropic

456   turbulent regime (Heilman *et al.*, 2015). The mean $\overline{w'^2}$ for all the sonic anemometers is 0.0597

457   m^{2}s^{-2} for the pre-burn period, 0.0931 m^{2}s^{-2} for the burn period, and 0.052 m^{2}s^{-2} for the post-burn

458   period, which yields an anisotropy ratio of 0.042, 0.036, 0.021 for the pre-burn, burn and post-

459   burn periods, respectively. As the anisotropy ratios are well below 1/3 in all three periods, the

460   turbulence regime just above the combustion zone remains anisotropic at all time. It is worth

461   noting that in contrary to the belief that the increase in vertical velocity variance in response to

462   the surface heating during the burn should act to move turbulence towards a more isotropic

463   regime, the ratio here is slightly smaller during the burn period than the pre burn period largely

464   because the fire-induced increase in the cross-stream velocity variance is larger than the increase

465   in the vertical velocity variance. Heilman and Bian (2015) calculated the anisotrophy ratios at 3

466   m above ground for two forest understory fires. The ratio decreased from 0.118 to 0.0718 from

467   pre-burn to burn in one experiment, but increased from 0.089 pre-burn to 0.13 in another

468   experiment. Since the sonic anemometers located on the western and southern sides of the burn

469   plot show no clear increase in $\overline{w'^2}$, the anisotropy ratio is also calculated for each sonic to verify

470   that the mean values did not mask anisotropy variations at individual locations in the burn plot.

471   No individual sonic anemometer reaches a ratio of 1/3, and the highest individual ratio (0.133) is

472   found at sonic anemometer A4 during the burn period. This result indicates that overall, the *TKE*

473   just above the combustion zone is highly anisotropic and is dominated by the horizontal

474   components for this burn. This result is not surprising as the sonic anemometers are located only

475   2.5 m above ground where horizontal turbulence would be expected to dominate over vertical

476   turbulence (Heilman *et al.*, 2015).

477

478   **3.3 Fire-Induced Shear Stress**

479   To address the question on how the surface fire alter turbulent momentum transfer

480   between the combustion zone and the atmosphere above, we next explore fire-induced changes

481   to turbulent momentum fluxes or shear stress measured by friction velocity described in Eq. (4).

21

482 Figure 10 shows time series of 1-minute averaged u_*^2 and the streamwise $\overline{u'w'}$ and cross-

483 stream $\overline{v'w'}$ stress components (the momentum flux), measured by each of the sonic

484 anemometers for the three periods. Kinematic momentum fluxes and u_*^2 are similar across all

485 the sonic anemometers during the pre-burn period, although three of the northernmost

486 instruments (A2, A3, and A4) indicate a negative spike in $\overline{u'w'}$ just before the start of the burn

487 period. These spikes contribute to an increase in u_*^2 at this time as well. It is not clear what

488 caused these features, but candidates include an anomalous burst of wind along the northern edge

489 of the burn plot and possible contamination of the wind data by activities of the burn managers

490 as they prepared to ignite the fire.

491 During the burn period, the values of $\overline{u'w'}$ and $\overline{v'w'}$ increase somewhat, leading to

492 increases in the u_*^2 values. The fire-induced changes generally increase in magnitude from west

493 (left) to east (right) and south to north, consistent with the fire-spread pattern. The largest

494 increase occur at the easternmost (right) locations, particularly A4 and C4 where u_*^2 values

495 nearly doubled. The smallest increases are not found at the westernmost locations, but at C2 and

496 D2. With a few exceptions, $\overline{u'w'}$ and $\overline{v'w'}$ are negative in the beginning of the burn period,

497 turning positive later in the period. The $\overline{u'w'}$ values exhibit the largest burn period variation at

498 A4, followed by B4, and similar patterns are observed for $\overline{v'w'}$. Overall, variations in u_*^2 suggest

499 an increase in shear stress magnitude in the burn period compared to the pre-burn period, with

500 the easternmost sonic anemometers recording 1-minute averaged values that are far greater than

501 the westernmost sonic anemometers.

502 During the post-burn period, some sonic anemometers (A2, B2, C1, C2, D2) recorded

503 higher u_*^2 than during the burn period, while others (A1, B1, B3, C2, C3, D3) recorded values

504   similar to the burn period. In either case, the average values are larger than during the pre-burn

505   period. The maximum post-burn values among all the sonic anemometers occur at A2 for u_*^2

506   and $\overline{v'w'}$ and C1 for $\overline{u'w'}$, both of which are larger than their burn-period peaks.

507   The overall distributions of u_*^2, $\overline{u'w'}$, and $\overline{v'w'}$ from all 16 sonic anemometers are

508   depicted in Figure 11. During the pre-burn period, $\overline{u'w'}$ is negative, with a mean value of -0.015

509    $m^2\ s^{-2}$, indicating an overall downward transfer of higher streamwise momentum air, which is

510   expected as wind speed usually increases with height. The mean of the cross-stream momentum

511   flux $\overline{v'w'}$ is near zero (0.007 $m^2\ s^{-2}$). However, the spread of the two components is similar, with

512   standard deviations of 0.057 $m^2\ s^{-2}$ and 0.046 $m^2\ s^{-2}$ for $\overline{u'w'}$ and $\overline{v'w'}$, respectively. The pre-burn

513   stress u_*^2 of 0.061 $m^2\ s^{-2}$ ($u_* = 0.25\ m^2\ s^{-2}$) is typical for daytime surface layers.

514   An increased in the downward (upward) transfer of higher streamwise (cross-stream)

515   momentum is observed during the burn period as the median values become more negative for

516    $\overline{u'w'}$ and more positive for $\overline{v'w'}$. However, the mean values change little from the pre-burn

517   period. The spread is doubled from a standard deviation of 0.046 to 0.098 $m^2\ s^{-2}$ for $\overline{u'w'}$ and

518   nearly tripled from 0.05 to 0.124 $m^2\ s^{-2}$ for $\overline{v'w'}$. The stronger upward transfer of cross-stream

519   momentum is consistent with the generation of cross-stream wind and updrafts in the vicinity of

520   the surface fire. Despite this overall fire-induced increase in $\overline{v'w'}$, the distribution of the cross-

521   stream momentum is negatively skewed by large negative outliers, suggesting occasional transfer

522   of higher cross-stream momentum by downdrafts near the vicinity of the fire. Both the mean and

523   standard deviation of u_*^2 values are doubled to 0.13 m^2s^{-2} and 0.086 m^2s^{-2}, respectively, over the

524   pre-burn values. The peak 1-min averaged values of u_*^2 exceed 0.4 m^2s^{-2} (or a friction velocity

525   of 0.6 $m\ s^{-1}$), which is 2.5 times larger than the pre-burn values. Clements *et al.* (2008) also

526   observed a three-fold increase in friction velocity in their experiment involving a high intensity

527   grass fire, although the absolute values of the friction velocity in their experiment were five

528   times larger (1 and 3 m s^{-1} before and during the fire) than the current experiment.

529   The mean post-burn $u_*{}^2$ value (0.10 m^{2}s^{-2}) is lower than that of the burn period but still

530   higher than the pre-burn value, driven primarily by the cross-stream component. The values of

531   the $\overline{v'w'}$ (0.0471 m^2 s^{-2}) in the post-burn period is more than six times the pre-burn average

532   (0.0072 m^{2}s^{-2}), with a standard deviation (0.069 m^{2}s^{-2}) that is between the pre-burn period

533   (0.046) and burn period (0.096) values. The mean friction velocity therefore does not return to

534   the pre-burn average, although it is lower than the average during the burn period. Other

535   experiments (e.g. Clements *et al*, 2008; Heilman, *et al.* 2019) noted a return of friction velocity

536   to pre-burn values soon after the passage of the fire front, during a period when smoldering was

537   occurring. The results of this analysis suggest that friction velocities do not quickly return to pre-

538   burn values on all fires.

539

540   **3.4 Fire-Induced Turbulent Heat Flux**

541   We proceed to examine the impact of the fire on turbulent heat flux. Time series of 1-

542   minute average turbulence sensible heat flux $\overline{T'w'}$ for each sonic anemometer are shown in

543   Figure 12 for the three periods, which also shows the overall distribution of heat fluxes for all the

544   sonic anemometers. In the pre-burn period, the sonic anemometers recorded background $\overline{T'w'}$

545   values that averaged around 5.25×10^{-2} °C m s^{-1} (or 52.7 W m^{-2}after multiplying by the density

546   and heat capacity of air), with a standard deviation of 3.41×10^{-2} °C m s^{-1} (34 W m^{-2}). During the

547   burn period, a fire-induced increase in $\overline{T'w'}$ is evident at all but the westernmost sonic

548   anemometers (A1, B1, C1, and D1), with larger increases appearing at the easternmost locations.

549   The largest $\overline{T'w'}$ values generally occur early in the burn period, with the A4 sonic having the

550   largest $\overline{T'w'}$ value of 2.13 °C m s^{-1} (2.138 kW m^{-2}). Based on the IR imaging (Figure 4), after the

551   first three minutes of the burn period there is a slight shift in the burn direction towards the

552   southeastern side of the plot. This shift in direction is apparent in the time series for the D4 sonic

553   anemometer, which is located on the southeastern corner of the burn plot, where elevated $\overline{T'w'}$

554   values are recorded late in the burn period, at a time when the values have dropped at most of the

555   other sonic anemometers. The overall distribution of the burn-period $\overline{T'w'}$ is skewed by larger

556   values since the plot mean was 0.268 K m s^{-1} (269 W m^{-2}) but the median was just 0.0974 °C m

557   s^{-1}(98 W m^{-2}).

558   Values of $\overline{T'w'}$ during the post-burn period quickly drop back to just slightly above the

559   pre-burn values, with a mean of 6.35×10^{-2} °C m s^{-1} (64 W m^{-2}) and a standard deviation of

560   3.76×10^{-2} °C m s^{-1}(38 Wm^{-2}). However, the post-burn period contains several outliers (above the

561   99.3% percentile), indicating the influence of smoldering on some of the sonic anemometers

562   even after the fire has exited the burn plot. A specific example of the smoldering effect is the D4

563   sonic anemometer, where the post-burn $\overline{T'w'}$ (0.126 °C m s^{-1} or 126 W m^{-2}) is about twice the

564   pre-burn value. The overall modest increase of $\overline{T'w'}$ in the post-burn period compared to the pre-

565   burn period was also observed in the two wildland fire experiments described in Heilman *et al.*

566   (2019).

567

568   **3.5 Quadrant Analyses**

569   **3.5.1 Turbulent heat fluxes**

570   The analysis above provided a quantitative assessment of fire-induced changes to the

571   turbulent heat and momentum fluxes through comparisons of flux values between the pre-burn

572   and the burn periods. However, such analysis cannot reveal what types of heat or momentum

573   transfer events are mostly affected by the fire. We apply the quadrant analysis method (also

574   known as sweep-ejection analysis) described earlier (Table 1) to the observed turbulent fluxes to

575   provide additional insight into how the fire changes the composition of heat and momentum

576   fluxes. By partitioning the total heat and momentum fluxes into four quadrants representing

577   different types of flux events, the quadrant or sweep-ejection analysis allows for the delineation

578   of the fire influence on specific types of turbulent heat and momentum transfer processes.

579   Figure 13 shows the relative contributions and the proportional number of occurrence of

580   the different heat-flux events (i.e., sweeps, ejections, outward interactions and inward

581   interactions) during each period, observed by each of the 16 sonic anemometers. During the pre-

582   burn period, the partitioning among the four types of events (see Table 1) by contribution and

583   proportion exhibits little variation across the 16 sonic anemometers. At all locations, the ejection

584   and sweep dominate, accounting for over 60% of the total events, with sweep being slightly

585   larger. The rest is split between outward interaction and inward interaction events, with the

586   former slightly outnumbering (20-23%) the latter (14-19%). A similar partitioning is observed

587   for the event contributions for the heat fluxes, but the ejection events, despite being slightly less

588   frequent, contribute more to the heat flux than do the sweep events. This apparent inconsistency

589   between the partitioning of the event number and the event contribution suggests that ejection

590   events likely involve larger eddies and stronger heat transfer compared to sweep events. This

591   pre-burn period partitioning is similar to previous ambient daytime measurements observed in

592   other studies (e.g., Heilman *et al.*, 2021).

593   The burn period is marked by substantial heterogeneity across the 16 sonic anemometers.

594   Despite differences in the magnitudes of contributions to the heat fluxes amongst the sonic

595   anemometers, the increases in the overall positive mean heat flux during the burn period can be

596   largely attributed to increases of ejection events that contribute to positive heat fluxes through

597   upward transfer of warmer air from the combustion zone to the atmosphere above. There is also

598   an increase in the negative contribution from inward interaction events, which represents the

599   downward transfer of warmer air from the atmosphere to the combustion zone. The contributions

600   to the overall mean heat flux by the other two types of events, sweep and outward interaction,

601   show little change from the pre-burn to the burn periods, which suggests that the turbulent heat

602   transfer processes represented by these types of events, namely downward transfer of colder air

603   from above to the surface or upward transfer of colder air from the combustion zone to the

604   atmosphere, are not very sensitive to the presence of a low-intensity fuel-bed-scale surface fire.

605   Compared to the partitioning in event contribution, the fire-induced changes to the

606   partitioning in event number are less clear. In general, the sonic anemometers that show an

607   increase in the contribution by inward interaction events also exhibit an increase in the number

608   of inward interaction events from the pre-burn to the burn periods. However, an increased

609   contribution to the overall mean heat flux by ejection events does not correspond to an increase

610   in the number of the ejection events. The increased number of sweep events are in agreement

611   with the increased sweep contributions at several sonics (A2-A4 and B2-B4), although the sweep

612   contributions are overwhelmed by that of the ejection contributions at these sonic anemometers.

613   A key finding from this heat flux sweep-ejection analysis is that turbulent heat fluxes

614   during the burn period are overwhelmingly dominated by ejection events, but there is usually a

615   small or no increase in the number of ejection events. This suggests that the presence of a low-

27

616 intensity fuel-bed-scale fire does not necessarily produce more upward turbulent heat transfer

617 events, but instead, it produces stronger events that quickly transfer and diffuse the sensible heat

618 generated by combustion into the ambient atmosphere above.

619 During the post-burn period, most sonic anemometers show vertical heat flux values that

620 are smaller than the burn period but still larger than the pre-burn period. The largest contribution

621 to the overall mean heat flux is usually from sweep events, accompanied also by an increase in

622 the number of the events, indicating the occurrence of many events where cold air is transferred

623 downward. The post-burn period also exhibits an increase in the heat-flux contributions from

624 outward interaction events, which represent downward transfer of warm air. Similar to the burn

625 period, inward interaction events, both in contribution and number, vary considerably across the

626 sonic array.

627 Figure 14 shows the partitioning of both the event number and the event contribution to

628 turbulent heat fluxes using data from all 16 sonic anemometers, which highlights more clearly

629 how the fire modifies the overall heat flux regime. Similar to the heat flux quadrant analysis for

630 individual sonic anemometers, the heat flux events averaged across the sonic anemometer array

631 for the pre-burn period is dominated by sweep (32%) and ejection (28%) events. Inward

632 interaction events occur with the least proportion (17%), followed by outward interaction events

633 (23%). The sweep and ejection events, which contribute to positive heat fluxes, are much larger

634 in magnitude than the negative heat flux contributions from the inward and outward interaction

635 events. The dominance of sweep and ejection events for the turbulent heat fluxes during the pre-

636 burn period follows observations made in previous studies (Heilman *et al.*, 2021).

637 The combined proportions of sweep and ejection events (both contributing to positive

638 heat fluxes) and the outward and inward interaction events (both contributing to negative heat

639   fluxes) remain similar between the burn and the pre-burn period. However, between the two

640   types of events in each group, one (sweep, inward interaction) increases and the other (ejection,

641   outward interaction) decreases in proportion. Previous fire experiments also reported an increase

642   in sweep events and a generally proportional decrease in ejection events (Heilman *et al.*, 2021),

643   but the magnitudes of the changes are larger than what is observed here, likely because the

644   previous fires are more intense. Additionally, modest changes in the partitioning of the event

645   number and contributions for this fire could be a byproduct of combining data from sonic

646   anemometers that are not strongly affected by the fire front (i.e. the westernmost sonic

647   anemometers) with those that experience more substantial changes.

648   The large changes in the contributions of the heat flux events during the burn period

649   suggest that this fire has greater impacts on the event contributions to the mean turbulent heat

650   fluxes than on the event number. Specifically, ejection event contributions dominate in the burn

651   period, making up 70.4% of the total contribution, while sweep and outward interaction

652   contributions decrease by a third and a sixth, respectively, compared to their contributions during

653   the pre-burn period. The magnitude of the contribution from inward interaction events increases

654   slightly but is quite similar to the contribution during the pre-burn period.

655   Heat flux events in the post-burn period more closely resemble the pre-burn period than

656   the burn period, but the event contributions and the event number do not return entirely to their

657   pre-burn values. As noted in the analyses of *TKE* and kinematic heat flux (Figures 9 and 11), this

658   result is consistent with smoldering occurring in the burn plot during the post-burn period. The

659   sweep event contribution during the post-burn period is 1.5 times higher than during the pre-burn

660   period and 1.3 times higher than during the burn period. Compared to the pre-burn values, the

661   post-burn period event contributions are slightly higher for outward interaction events and

662   slightly lower for ejection and inward interaction events. Overall, the post-burn period is

663   dominated by contributions from sweep events (37.7%), which is followed by ejection event

664   (25.3%) although lower than pre-burn values. These results differ somewhat from the Heilman *et*

665   *al.* (2021) in that they reported both sweep and ejection events returning to pre-burn values,

666   while only ejection events return to pre-burn values for this fire.

667

668   **3.5.2 Turbulent momentum fluxes**

669   Quadrant analysis is also applied to partition the vertical turbulent kinematic flux of

670   horizontal momentum $\overline{S'w'}$ into four different types and the results for each of the 16 sonic

671   anemometers are shown in Figure 15. During the pre-burn period, the overall mean momentum

672   fluxes are negative at all but two sonic anemometers (C1, C2) where the flux is slightly positive.

673   Between the two types of events that contribute to negative momentum fluxes, the sweep events

674   (downward transfer of higher horizontal momentum air from the atmosphere to the combustion

675   zone) contribute more than the ejection events (upward transfer of lower horizontal momentum

676   air from the combustion zone to the atmosphere above), which is consistent with the slightly

677   higher number of sweep events than ejection events. Between the two types of events that

678   contribute to positive momentum fluxes, the outward interaction events (upward transfer of

679   higher horizontal momentum air from the combustion zone to the atmosphere above) contribute

680   more than the inward interaction events (downward transfer of lower horizontal momentum air

681   from the atmosphere to the combustion zone), although the number of the inward and outward

682   interaction events is similar .

683   The changes from the pre-burn period to the burn period vary substantially by location,

684   but the sign of the overall mean momentum fluxes remains unchanged at most locations. The

685   most pronounced and consistent change across the anemometer array is a substantial increase in

686   the proportional number of inward interaction events and, to a lesser degree, the contribution

687   from these events. The ejection events also exhibit an increase in the number and the

688   contribution at most of the sonic anemometer locations. There is a general decrease in the

689   number of sweep and outward interaction events, but the contributions are not consistent, with

690   some sonic anemometers showing an increase while others experience a decrease in contribution.

691   An exception to the above general observations between the pre-burn and burn periods is

692   B4, where the overall momentum flux shifts from negative to positive due to an increase in

693   outward interaction contribution by as much as 5 times the pre-burn magnitude. The amount of

694   increase in the contribution from the outward interaction events, however, does not match the

695   small increase (approximately 10%) in the event number, which suggests that the increase in the

696   overall momentum flux magnitude at this location is likely due a small number of extremely

697   strong events of upward transfer of higher horizontal momentum air associated with large,

698   energetic eddies generated by the surface fire.

699   The large heterogeneity in the event contribution values for the momentum fluxes across

700   the sonic anemometer array during the burn period dissipated substantially into the post-burn

701   period. The event contribution and event number distributions once again become less dependent

702   on the locations of the sonic anemometers. Despite this tendency to return to the pre-burn

703   distribution, the post-burn period experiences larger contributions from, and higher number of

704   ejection and inward interaction events than sweep and outward interaction events, which is

705   opposite to the pre-burn period and similar to the burn period.

706   Figure 16 shows a quadrant analysis that combines data from all the sonic anemometers,

707   which allows for an assessment of how the fire modified the momentum flux turbulence regime

708   for the entire burn plot. Overall, sweep (31.9%) and outward interaction (26.6%) events

709   dominate the momentum flux contributions in the pre-burn period. The increases in the

710   proportion of inward interaction and ejection events from the pre-burn to the burn periods make

711   the contributions more balanced across the four quadrants, suggesting that the different event

712   contributions are more similar to each other during the burn than the pre-burn period. In the post-

713   fire period, inward interaction events contribute more to the mean momentum flux (25.7%) than

714   during the pre-fire period (18.1%). The event number distributions in the combined analysis

715   echoes the results from the individual sonic anemometers, with the pre-burn period showing

716   similar values for all four quadrants, a sharp increase in inward interaction events and decrease in

717   outward interaction events during the burn period, and fewer inward interaction events during the

718   post-burn period than during the burn period but more numerous than during the pre-burn period.

719   The results of the quadrant analysis of momentum fluxes presented above are somewhat

720   different from those of previous studies involving operational-scale prescribed burns. Heilman *et*

721   *al.* (2021) showed that during an intense grass fire and two low-intensity forest understory fires,

722   there can be substantial increase in the number and contribution of sweep and outward

723   interaction events and that the increase in the positive momentum flux from outward interaction

724   events largely offset the increase in the negative flux associated with sweep events. Whereas in

725   the small fuel-bed scale burn here, inward interactions occur most frequently, followed by

726   ejection events. However, the ejection event contributions to the mean momentum flux are larger

727   (32.3%), with the inward interaction event contributions (24.2%) more similar to the outward

728   interaction (23.4%) contributions. The feature of increased frequency of inward interaction

729 events and their increased contribution to the mean momentum flux compared to previous burns

730 is further observed in the post-burn period.

731 The event number and event contributions during the post-burn period also differ with

732 increased ejection and inward interactions events, 32.8% and 20.6%, while the large-scale burns

733 in Heilman *et al.* (2021) showed a closer return to pre-fire periods, with sweep and ejection

734 events making up the majority of event number and contributions. The contributions from sweep,

735 inward interaction, and ejection events remain elevated during the post-burn period, while the

736 contributions from outward interaction decrease during post-burn to values lower than the values

737 of the pre-burn period.

738

4. Summary

740 This study presents atmospheric turbulence observed using a 4×4 array of fast-response

741 3D sonic anemometers during a low-intensity fire experiment on a 10 m x 10 m burn plot in the

742 Silas Little Experimental Forest in New Jersey, USA. The density of turbulence measurements is

743 unprecedented for fire experiments, allowing for a deeper analysis of heterogeneities as the

744 surface line-fire spread through the burn plot than was previously possible. The analysis focuses

745 on assessments of the fire impacts on turbulence intensity, as measured by *TKE*, turbulent

746 momentum flux or shear stress as measured by friction velocity, and turbulent heat flux.

747 The influence of the low-intensity surface line-fire on the atmosphere above the

748 combustion zone is evidenced by an increase in temperature up to 20 ºC, the generation of strong

749 updrafts up to 6 m s^{-1} and downdrafts up to -5 m s^{-1}and a decrease in the streamwise velocity

750 coupled with an increase in the cross-stream velocity indicting horizontal convergence in the

751   vicinity of the fire front. The observed fire exhibited behavior more consistent with a buoyant

752   plume than mechanically forced rising motion resulting from converging surface air. The

753   influence of the fire on horizontal velocity components persisted longer after fire front passage

754   while the influence on vertical velocity subsided rapidly behind the fire front.

755   The fire modified turbulence characteristics at the fuel bed-atmosphere interface. There

756   was an increase in the turbulence intensity, with *TKE* values 2-3 times higher than the ambient

757   environment, due primarily to the increase in cross-stream velocity variance and, to a lesser

758   degree, the increase in the vertical velocity and streamwise velocity variance. Heilman *et al.*

759   (2017) also reported two to threefold increases in *TKE* values during two operational-scale low-

760   intensity forest understory prescribed fires. It is interesting to note that this increase in *TKE* is

761   only slightly smaller than what was observed during the intense grass fire during FireFlux

762   (Clements *et al.*, 2007), although the magnitude of *TKE* of the intense grass fire is substantially

763   larger than that of the low-intensity fires. Despite this increase in *TKE*, the value of *TKE* was still

764   smaller than what is expected in an environment of substantial turbulence. Additionally, despite

765   the increase in the vertical velocity variance during the fire, the *TKE* was still dominated by the

766   horizontal velocity variance, indicating that the turbulence regime remained anisotropic

767   (anisotropic ratio << 1/3) above the combustion zone of this low-intensity fuel-bed-scale surface

768   fire.

769   The fire enhanced upward sensible heat fluxes substantially by as much as 40 times the

770   flux in the ambient atmosphere (from 50 W m^{-2} to 2 kW m^{-2}). This change in the sensible heat

771   flux is largely attributable to an increased contribution of upward transfer by turbulent eddies of

772   warmer air from the combustion zone to the atmosphere above, which is also known as ejection

773   events for vertical turbulent heat transfer. This increase in the contribution of the ejection events

34

774   to turbulent heat fluxes was not caused by a corresponding increase in the number of ejection

775   events that changed little from the pre-burn to burn periods. This mismatch between the ejection

776   event contribution and event number suggests that the presence of a low-intensity fuel-bed-scale

777   fire may not necessarily produce more upward turbulent heat transfer events, but rather, it can

778   produce strong ejection events associated with large, energetic eddies. The warmer air

779   transported upward by the ejection events can also be transported downward by inward

780   interaction events, which also increased somewhat during the fire.

781   Compared to the turbulent heat flux, the impact of the fire on turbulent momentum flux

782   or shear stress was less pronounced. In general, an increase in momentum fluxes was observed

783   during the burn, with friction velocity, a measure of total shear stress on horizontal wind, 2-3

784   times the ambient value (from ~ 0.25 ms^{-1} to 0.6 ms^{-1}). Previous studies of operational-scale

785   grass fire or forest understory fires also found up to a 3-fold increase in friction velocity despite

786   that the scale of this fire is much smaller than the previous fires and that the absolute values of

787   friction velocity during the intense grass fire were 5 times higher than the low-intensity fire here

788   (Clements *et al.*, 2007; Heilman *et al.,* 2017; 2021). The fire was accompanied by an increase in

789   the downward transfer of lower horizontal momentum air, also known as inward interaction

790   events, along with a smaller increase in the upward transfer of lower horizontal momentum air

791   referred to as ejection events. This finding differs from previous observations during an

792   operational-scale forest understory fire where an increase in sweep (downward transfer of higher

793   horizontal momentum air) and outward interaction (upward transfer of higher horizontal

794   momentum air) contributions to the mean momentum fluxes were detected (Heilman *et al.*,

795   2021).

796   Perhaps the most significant finding from this study is the large variations in the observed

797   fire-induced perturbations across the sonic anemometer array in the burn plot. The anemometers

798   on the western side of the burn plot where a surface line-fire was ignited picked up very weak or

799   no signals of the fire despite the proximity to the initial fire line. In contrast, the sonic

800   anemometers in the center or eastern side of the burn plot picked up clear fire signals. Although

801   the features of fire-induced turbulence regime (e.g., anisotropy, sweep-ejection dynamics)

802   revealed by the sonic anemometers are similar, the magnitudes vary with downwind distance and

803   the relative position of the sonic anemometers to the impinging fire front. Considering the size of

804   the burn plot (10 m x 10 m) and the homogeneity of consumed fuels, this finding suggests that

805   considerable care should be taken when comparing, contrasting, and combining data from

806   multiple fires or from multiple instruments on the same fire to ensure that significant fire signals

807   are not being over- or under-represented in the analyses that inform the conclusions of the

808   studies. This also calls into question of using numerical simulations from coupled atmosphere-

809   fire behavior models with horizontal grid spacing $\geq$10 m. The results presented here suggest that

810   1-2 m grid spacing is necessary for model simulations to capture atmospheric turbulent

811   circulations that have spatiotemporal scales similar to the scales associated with flame dynamics

812   in the combustion zone.

813   Future work will compare results from this case with those of other burns in the 10 m x

814   10 m burn series to delineate the effect of fuel and ambient atmospheric conditions on fire-

815   atmosphere interactions and with results from other prescribed-fire experiments to help scale up

816   or scale down the results between small-scale and operational scale fires. Future work will also

817   include the reanalysis of 10 Hz sonic anemometer data from other fire experiments using some

818   or all of the methodologies employed here, which could contribute to the identification and

819 documentation of a series of steps, protocols, standards, and methodologies by which 10-Hz

820 sonic anemometer data collected during fire experiments can be compared and contextualized.

821 Additionally, the data collected from the other instruments deployed during the SERDP fuel-bed-

822 scale fire experiments should be included in future analyses. Spectral and co-spectral analyses

823 should be performed to help understand the temporal and spatial scale of turbulence regimes at

824 the fuel-bed and atmosphere interface.

825 Because the burn period was chosen to be between the time when the first and the last

826 sonic anemometers have temperatures satisfying the threshold value (eight standard deviations in

827 these analyses), the burn period included time after the fire has passed the sonic anemometer

828 location, which likely yielded an underestimation of the fire effect. Similarly, the inclusion of all

829 16 sonic anemometers in the analysis, including those that registered little fire signal, likely

830 contributed to an underestimation. Consequently, fire-induced turbulent circulations and the

831 associated turbulent heat and momentum fluxes are likely to be stronger than what has been

832 reported here.

833

834 **Acknowledgements**

841

Code and Data Availability

Python language was used for all analyses and data management, with the Pandas package

(https://zenodo.org/record/7037953#.Yw-at3bMIp4) used for data processing, NumPy package

(https://numpy.org/) used for most statistical calculations and Matplotlib visualization package

(https://matplotlib.org/) used for plotting, , all of which are open source packaged in the Python

environment. The computer codes and the data are hosted on software sharing and version

control website and service GitHub. https://github.com/JosephSeitz/SERDP-10x10meter-Burn-

Cleaner.

All data used in this study are publicly archived and available via the USFS Data Archive (in

press, links to be included in revised version).

852

Author Contributions

All authors contributed to the research design. K.C., N.S., M.G., M.P., R.H. and E.M. conducted

the fire experiment and collected the data. J.C. and M.P., with assistance from K.C., did the

initial process and formatting of the data. J.S., with assistance and guidance from J.J.C. and

discussions and feedback from S.Z., W.H., X.B. M.K., performed the data analysis and produced

all the plots. S.Z. wrote the manuscript. M.G., W.H., K.C. and N.S. edited the manuscript.

859

References

Amaya, M.A. and Clements C.B. (2020) Evolution of plume core structures and turbulence during a wildland fire experiment. *Atmosphere,* **11**, 842.

Bennie, J., Huntley, B., Wiltshire, A., Hill, M.O. and Baxter, R. (2008) Slope, aspect and climate: Spatially explicit and implicit models of topographic microclimate in chalk grassland. *Ecological Modeling,* **216**, 47-59.

Billmire, M., Frenc, N.H.F., Loboda, T., Owen, R.C. and Tyner, M. (2014) Santa Ana winds and predictors of wildfire progression in southern California, *International Journal of Wildland Fire*, **23**, 1119-1129.

Calviño-Cancela, M, Chas-Amil, M.L., García-Martínez, E.D. and Touza, J. (2017) Interacting effects of topography, vegetation, human activities and wildland-urban interfaces on wildfire ignition risk. *Forest Ecology and Management,* **397**, 10-17.

Campbell-Lochrie, Z., Walker-Ravena, C., Gallagher, M., Skowonski, N., Mueller, E., Hadden, R.M. (2021) Investigation of the role of bulk properties and in-bed structure in the flow regime of buoyancy-dominated flame spread in porous fuel bed. Fire Safety Journal, 120, https://doi.org/10.1016/j.firesaf.2020.103035

Campbell-Lochrie, Zakary J.; Hadden, Rory M.; Mueller, Eric V.; Walker-Ravena, Carlos; Gallagher, Michael R.; Clark, Kenneth L.; Hom, John L.; Kremens, Robert L.; Cole, Jason A.; Patterson, Matthew M.; Everland, Alexis I.; Skowronski, Nicholas S. 2022. Multi-scale analyses of wildland fire combustion processes: Small-scale field experiments -

Transportable Analyzer for Calorimetry Outside (TACO). Fort Collins, CO: Forest Service
Research Data Archive.

Carrier, G.F., Fendell, F.E. and Wolff, M.F. (1991) Wind-aided fire spread across arrays of
discrete fuel elements. I. Theory. *Combustion Science and Technology*, **75**, pp.31-51.

Clark, Kenneth L.; Gallagher, Michael R.; Mueller, Eric V.; Hadden, Rory M.; Walker-Ravena,
Carlos; Campbell-Lochrie, Zakary J.; Cole, Jason A.; Patterson, Matthew M.; Everland,
Alexis I.; Skowronski, Nicholas S. 2022a. Multi-scale analyses of wildland fire combustion
processes: Small-scale field experiments - three-dimensional wind and temperature. Fort
Collins, CO: Forest Service Research Data Archive.

Clark, Kenneth L.; Gallagher, Michael R.; Mueller, Eric V.; Hadden, Rory M.; Walker-Ravena,
Carlos; Campbell-Lochrie, Zakary J.; Cole, Jason A.; Patterson, Matthew M.; Everland,
Alexis I.; Skowronski, Nicholas S. 2022b. Multi-scale analyses of wildland fire combustion
processes: Small-scale field experiments - temperature profile. Fort Collins, CO: Forest
Service Research Data Archive.

Clark, K.L., Heilman, W.E., Skowronski, N.S., Gallagher, M.R., Mueller, E., Hadden, R.M., and
Simeoni, A. (2020) Fire behavior, fuel consumption, and turbulence and energy exchange
during prescribed fires in pitch pine forests. *Atmosphere,* **11**, 242.

Clark, T.L., Jenkins, M.A., Coen, J.L. and Packham, D.R., (1996) A coupled atmosphere-fire
model: Role of the convective Froude number and dynamic fingering at the fireline.
International Journal of Wildland Fire, **6**, pp.177-190.

Clements, C.B., and Seto, D. (2015) Observations of fire-atmosphere interactions and near-
surface heat transport on a slope. *Boundary-Layer Meteorology,* **154**, 409-426.

Clements, C.B., Kochanski, A.K., Seto, D., Davis, B., Camacho, C., Lareau, N.P., Contezac, J.,
Restaino, J., Heilman, W.E., Krueger, S.K. and Butler, B. (2019) The FireFlux II
experiment: a model-guided field experiment to improve understanding of fire–atmosphere
interactions and fire spread. *International Journal of Wildland Fire*, **28**, 308-326.

Clements, C.B., Kochanski, A.K., Seto, D., Davis, B., Camacho, C., Lareau, N.P., Contezac, J.,
Restaino, J., Heilman, W.E., Krueger, S.K., Butler, B., Ottmar, R.D., Vihnanek, R., Flynn,
J., Filippi, J.B., Barboni, T., Hall, D.E., Mandel, J., Jenkins, M.A., O'Brien, J., Hornsby, B.,
and Teske, C. (2019) The FireFlux II experiment: a model-guided field experiment to
improve understanding of fire–atmosphere interactions and fire spread. *International
Journal of Wildland Fire,* **28,** 308-326.

Clements, C.B., Zhong, S., Bian, X., Heilman, W.E., and Byun, D.W. (2008), First observations
of turbulence generated by grass fires. *Journal of Geophysical Research*, **113**, D22102.

Clements, C.B., Zhong, S., Goodrick, S., Li, J., Potter, B.E., Bian, X., Heilman, W.E., Charney,
J.J., Perna, R., Jang, M. and Lee, D. (2007) Observing the dynamics of wildland grass fires:
FireFlux—A field validation experiment. *Bulletin of the American Meteorological Society*,
88, 1369-1382.

Di. Christina, G., Gallagher, M., Skowonski, N., Simeoni, In, S.-K. (2022 Design and
implementation of a portable large-scale wind tunnel for wildfire research. *Fire Safety
Journal*, **131**, 103607.

Ebel, B.A. (2013) Simulated unsaturated flow processes after wildfire and interactions with slope
aspect. *Water Resources Research,* **49**, 8090-8107

Finney, M.A., Cohen, J.D., Forthofer, J.M., McAllister, S.S., Golner, M.J., Gorham, D.J., Saito, K., Akafuah, N.K., Adam, B.A., and English, J.D. (2015) Role of buoyant flame dynamics in wildfire spread. *Proceedings of the National Academy of Sciences,* **112**, 9833-9838.

Forthofer, J.M., and Goodrick, S.L. (2011) Review of vortices in wildland fire. *Journal of Combustion,* **2011**, Article ID 984363.

Gallagher, Michael R.; Skowronski, Nicholas S.; Hadden, Rory M.; Mueller, Eric V.; Clark, Kenneth L.; Campbell-Lochrie, Zakary J.; Walker-Ravena, Carlos; Kremens, Robert L.; Everland, Alexis I.; Patterson, Matthew M.; Cole, Jason A.; Heilman, Warren E.; Charney, Joseph J.; Bian, Xindi; Mell, William E.; Hom, John L.; Im, Seong-kyun; Kiefer, Michael T.; Zhong, Shiyuan; Simeoni, Albert J.; Rangwala, Ali; Di Cristina, Giovanni. (2022) Multi-scale analyses of wildland fire combustion processes: Small-scale field experiments – plot layout and documentation. Fort Collins, CO: Forest Service Research Data Archive

Heilman, W.E. (2021) Atmospheric turbulence in wildland fire environments: implications for fire behavior and smoke dispersion. *Fire Management Today. **79***, pp.24-29.

Heilman, W.E. and Bian, X. (2013) Climate variability of near surface turbulent kinetic energy over the United States: Implications for fire weather prediction. *Journal of Applied Meteorology and Climatology*, 52, 753-772.

Heilman, W.E., Barnerjee, T., Clements, C.B., Clark, K.L., Zhong, S., and Bian X. (2021) Observations of sweep-ejection dynamics for heat and momentum fluxes during wildland fires in forested and grassland environments. *Journal of Applied Meteorology and Climatology*, **60**, 185-199.

Heilman, W.E., Bian, X., Clark, K.L. and Zhong, S. (2019) Observations of turbulent heat and momentum fluxes during wildland fires in forested environments. *Journal of Applied Meteorology and Climatology*, **58**, pp.813-829.

Heilman, W.E., Bian, X., Clark, K.L., Skowronski, N.S., Hom, J.L. and Gallagher, M.R. (2017) Atmospheric turbulence observations in the vicinity of surface fires in forested environments. *Journal of Applied Meteorology and Climatology*, **56**, 3133-3150.

Heilman, W.E., Clements, C.B., Seto, D., Clark, K.L., Skowonski, N.S., and Hom, L.J. (2015) Observations of fire-induced turbulence regimes during low-intensity wildland fires in forested environments: Implications for smoke dispersion. *Atmospheric Science Letters*, **16**, 453-460.

Heilman W.E. and Bian, X. (2013)

Katul, G., Poggi, D., Cava, D., and Finnigan, J. (2006) The relative importance of ejections and sweeps to momentum transfer in the atmospheric boundary layer. *Bound.-Layer Meteor.*, **120**, 367–375.

Katul, G., Kuhn, G., Schieldge, J., and Hsieh, C.-I. (1997) The ejection sweep character of scalar fluxes in the unstable surface layer. *Bound.-Layer Meteor.*, **83**, 1–26.

Kitzberger, T., Falk, D.A., Westerling, A.L., and Swetnam T.W. (2017) Direct and indirect climate controls predict heterogeneous early-mid 21st century wildfire burned area across western and boreal North America. *PLOS ONE,* **12**, e0188486.

Kremens, Robert L.; Gallagher, Michael R.; Clark, Kenneth L.; Mueller, Eric V.; Hadden, Rory M.; Heilman, Warren E.; Charney, Joseph J.; Hom, John L.; Campbell-Lochrie, Zakary J.;

Walker-Ravena, Carlos; Everland, Alexis I.; Cole, Jason A.; Patterson, Matthew M.; Skowronski, Nicholas S. 2022. Multi-scale analyses of wildland fire combustion processes: Small-scale field experiments - fire radiative power. Fort Collins, CO: Forest Service Research Data Archive.

Littell, J.S., Peterson, D.L., Riley, K.L., Liu, Y. and Luce, C.H. (2016). A review of the relationships between drought and forest fire in the United States. *Global Change Biology,* **22**, 2353-2369.

Moody, M.J., Gibbs, J.A., Kruger, S., Mallia, D., Pardyjak, E.R., Kochanski, A.K., Bailey, B.N., Stoll, R. (2022) QES-Fire, a dynamically coupled fast-response wildfire model. International Journal of Wildland Fire, **31,** 306-325.

Mueller, E.V., Skowronski, N.,Clark, K., Gallagher, M., Kremens, R., Thomas, J.C., El Houssami, M., Filkov, A., Hadden, R.M., Mell, W.; et al. (2017) Utilization of remote sensing techniques for the quantification of fire behavior in two pine stands. *Fire Safety Journal*, **91**, 845–854, doi:10.1016/j.firesaf.2017.03.076.

Potter, B.E. (1996) Atmospheric properties associated with large wildfires. *International Journal of Wildland Fire* **6**, 71–76.

Potter, B.E. (2012): Atmospheric interactions with wildland fire behavior – I: Basic surface interactions, vertical profiles and synoptic structures. *International Journal of Wildland Fire*, **21**, 779-801.

Povak, N.A., Hessburg, P.F. and Salter, R.B. (2018) Evidence for scale-dependent topographic controls on wildfire spread. *Ecosphere,* **9**(10): e02443.

Seto, D., Strand, T.M., Clements, C.B., Thistle, H., and Mickler, R. (2014) Wind and plume
thermodynamic structures during low-intensity subcanopy fires. *Agricultural and Forest
Meteorology,* **198-199**, 53-61.

Seto D., Clements, C.B., and Heilman, W.E. (2013) Turbulence spectra measured during fire
front passage. *Agricultural and Forest Meteorology,* **169**, 195-210.

Seto, D., and Clements, C.B. (2011) Fire whirl evolution observed during a valley wind-sea
breeze reversal. *Journal of Combustion*, **2011**, 12pp https://doi.org/10.1155/2011/569475

Sharples, J.J. (2009) An overview of mountain meteorological effects relevant to fire behaviour
and bushfire risk. *International Journal of Wildland Fire* **18**, 737-754.

Sharples, J.J., McRae, R.H.D., Wilkes, S.R. (2012) Wind–terrain effects on the propagation of
wildfires in rugged terrain: Fire channelling. *International Journal of Wildland Fire,* **21**,
282-296.

Skowronski, N.S. (2021) Multi-scale analysis of wildland fire combustion processes in open
canopy forests using coupled iteratively informed laboratory-, field- and mode-based
approach. Final Technical Report, SERDP Project RC-2641. Available at
https://www.serdp-estcp.org/Program-Areas/Resource-Conservation-and-Resiliency/Air-
Quality/Fire-Emissions/RC-2641

Skowronski, Nicholas S.; Charney, Joseph J; Clark, Kenneth L.; Gallagher, Michael R.; Hadden,
Rory M.; Heilman, Warren E.; Hom, John L.; Kremens, Robert L.; Cole, Jason A.;
Campbell-Lochrie, Zakary J.; Walker-Ravena, Carlos; Mueller, Eric V.; Everland, Alexis
I.; Patterson, Matthew M. 2022a. Multi-scale analyses of wildland fire combustion

processes: Small-scale field experiments - infrared data. Fort Collins, CO: Forest Service
Research Data Archive.

Skowronski, Nicholas S.; Charney, Joseph J; Clark, Kenneth L.; Gallagher, Michael R.; Hadden,
Rory M.; Heilman, Warren E.; Hom, John L.; Kremens, Robert L.; Cole, Jason A.;
Campbell-Lochrie, Zakary J.; Walker-Ravena, Carlos; Mueller, Eric V.; Everland, Alexis
I.; Patterson, Matthew M. 2022b. Multi-scale analyses of wildland fire combustion
processes: Small-scale field experiments – terrestrial laser scans. Fort Collins, CO: Forest
Service Research Data Archive.

Skowronski, N., and Hom, J.L. (2015): Observations of fire-induced turbulence regimes during
low-intensity wildland fires in forested environments: Implications for smoke dispersion.
Atmospheric Sciences Letters, **16**, 453–460.

Stull, R.B., (1988) An introduction to boundary layer meteorology (Vol. 13). Springer Science &
Business Media.

Viegas, D.X., and Neto, L.P. (1991) Wall shear stress as a parameter to correlate the rate of
spread of a wind-induced forest fire. *International Journal of Wildland Fire,* **1**, 177–188.

Werth, P.A., Potter, B.E., Clements, C.B., Finney, M.A., Goodrick, S.L., Alexander, M.E., Cruz,
M.G., Forthofer, J.A., and McAllister, S.S. (2011) Synthesis of knowledge of extreme fire
behavior: For fire managers. General Technical Report PNW-GTR-854, US Department of
Agriculture, Forest Service, Pacific Northwest Research Station, Vol. I. Portland, OR, 144.

Table 1. Vertical turbulent transfer events and the associated quadrat designations.

Q	$\varphi'w'$	φ'	w'	Heat flux	Momentum flux
1	>0	>0	>0	Ejection: upward flux of warmer air	Outward Interaction: upward flux of lower horizontal momentum air
2	<0	<0	>0	Inward Interaction: downward flux of warmer air	Sweep: downward flux of higher horizontal momentum air
3	>0	<0	<0	Sweep: downward flux of cooler air	Inward Interaction: downward flux of lower horizontal momentum air
4	<0	<0	>0	Outward Interaction: upward flux of cooler air	Ejection: upward flux of higher horizontal momentum air

LIST OF FIGURES

Figure 10. Time series of 1-minute averaged friction velocity squared ($u_*{}^2$, pink pluses) and its two components, the streamwise kinematic momentum flux, $\overline{u'w'}$ (yellow circle) and the cross-stream kinematic momentum flux, $\overline{v'w'}$ (blue diamonds), for each of the 16 sonic anemometers. The vertical dashed black lines indicate the burn period determined by the first and last occurrence of $T' \geq 8\sigma$. Time is the minutes since the start of the pre-burn period.

Figure 11. Distributions of friction velocity squared ($u_*{}^2$) and its two components ($\overline{u'w'}$ and $\overline{v'w'}$) from all 16 sonic anemometers during the pre-burn, burn, and post-burn periods. The box represents the 25th and 75th percentile of the data, with data inside the whiskers representing *99.3%* of the data. The orange line in the boxes is the median value, the green triangle is the mean, and the blue shading is the density of values of the data.

Figure 12. Time series of 1-minute averaged heat flux for each of the 16 sonic anemometers (left) and the distribution of heat fluxes from all 16 sonic anemometers during the pre-burn, burn, and post-burn periods (right). The box represents the 25th and 75th percentile of the data, with data inside the whiskers representing *99.3%* of the data. The orange line in the boxes is the median value, the green triangle is the mean, and the blue shading is the density of values of the data.

Figure 13. Quadrant analysis of the instantaneous vertical kinematic turbulent heat fluxes showing the contributions to the total flux from (top row), and the percent of (bottom row) the four types of events: outward interaction (green), ejection (red), inward interaction (blue), and sweep (orange) for each of the 16 sonic anemometers during the pre-burn, burn, and post-burn periods. The black diamonds in the top row indicate the total heat flux values. The sonic anemometers are arranged from west to east roughly following the fire spread across the burn plot.

Figure 14. Quadrant analysis of the instantaneous vertical kinematic turbulent heat fluxes showing the contributions to the total flux from (top row), and the percent of (bottom row) the four types of events: outward interaction (green), ejection (red), inward interaction (blue), and sweep (orange) for all 16 sonic anemometers during the pre-burn, burn, and post-burn periods. The black diamonds in the top row indicate the total heat flux values. The sonic anemometers are arranged from west to east roughly following the fire spread across the burn plot.

Figure 15. Quadrant analysis of the instantaneous vertical kinematic turbulent fluxes of horizontal momentum showing the contributions to the total flux from (top row), and the percent of (bottom row) the four types of events: outward interaction (red), sweep (green), inward interaction (orange), and ejection (blue) for each of the 16 sonic anemometers during the pre-burn, burn, and post-burn periods. The black diamonds in the top row indicate the total flux values. The sonic anemometers are arranged from west to east roughly following the fire spread across the burn plot.

Figure 16. Quadrant analysis of the instantaneous vertical kinematic turbulent fluxes of horizontal momentum showing the contributions to the total flux from (top row), and the percent of (bottom row) the four types of events: outward interaction (red), sweep (green), inward

interaction (orange), and ejection (blue) for all 16 sonic anemometers during the pre-burn, burn, and post-burn periods. The black diamonds in the top row indicate the total flux values. The sonic anemometers are arranged from west to east roughly following the fire spread across the burn plot.
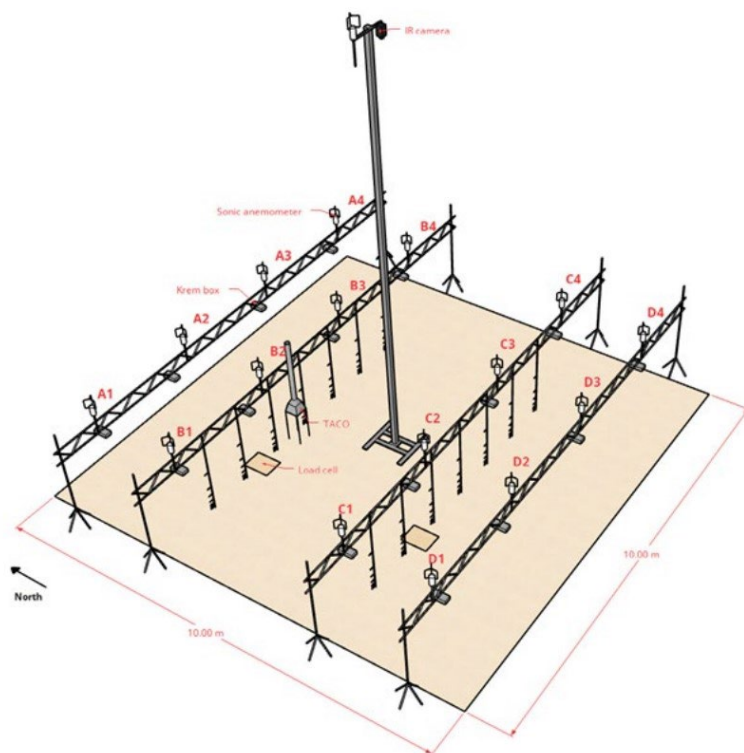
Figure 1. Sketch of the burn plot and the instruments deployed to the plot. The four capital letters (A, B, C and D) denote the four trusses and the four numbers (1, 2, 3, 4) refer to the 3D sonic anemometers on the trusses. Posts hanging on trusses B and C show the heights and location of thermocouples. The center post indicates the position of the infrared camera. The boxes next to the sonic anemometers indicate the radiometer/spectral camera pairs. The rectangular box on the ground indicates fuel cells for fuel loading estimation. The symbol near B2 indicates the TACO for emission data collection
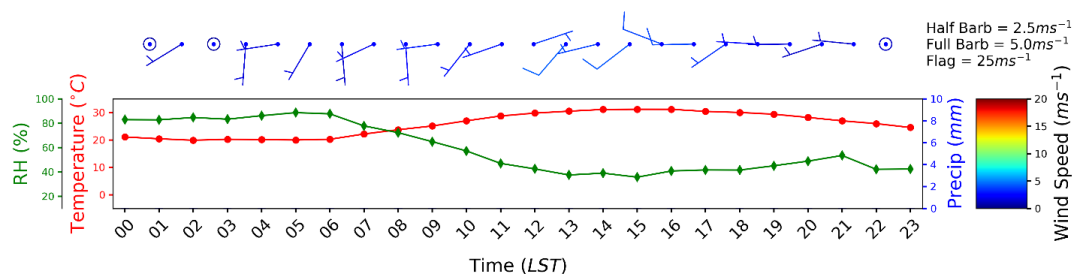
Figure 2. Surface meteorological condition on May 20, 2019, the day of the experimental burn, observed by the weather station approximately 200 m northeast of the burn plot.
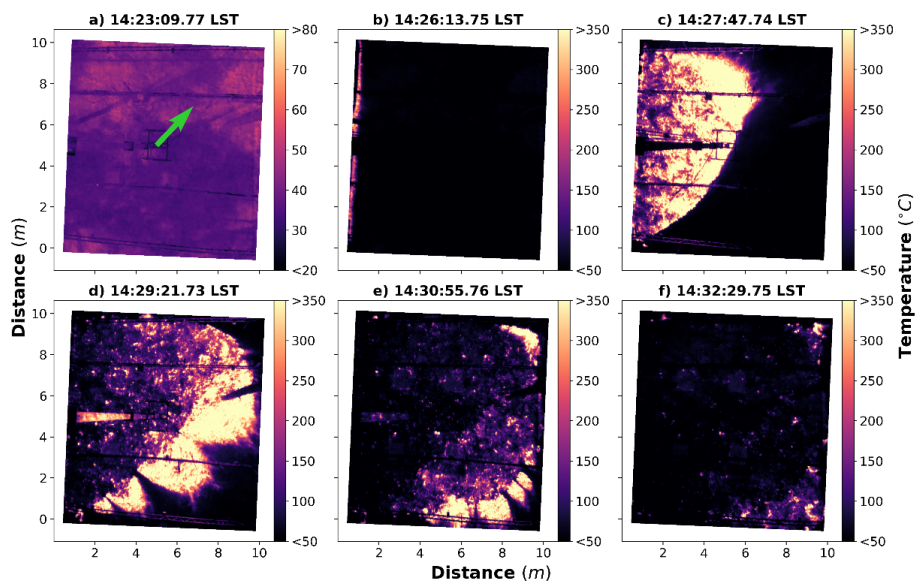
Figure 3. Infrared images taken at 10 m above the center of the burn plot showing fuel bed temperature before a), near b) and after c-f) ignition.
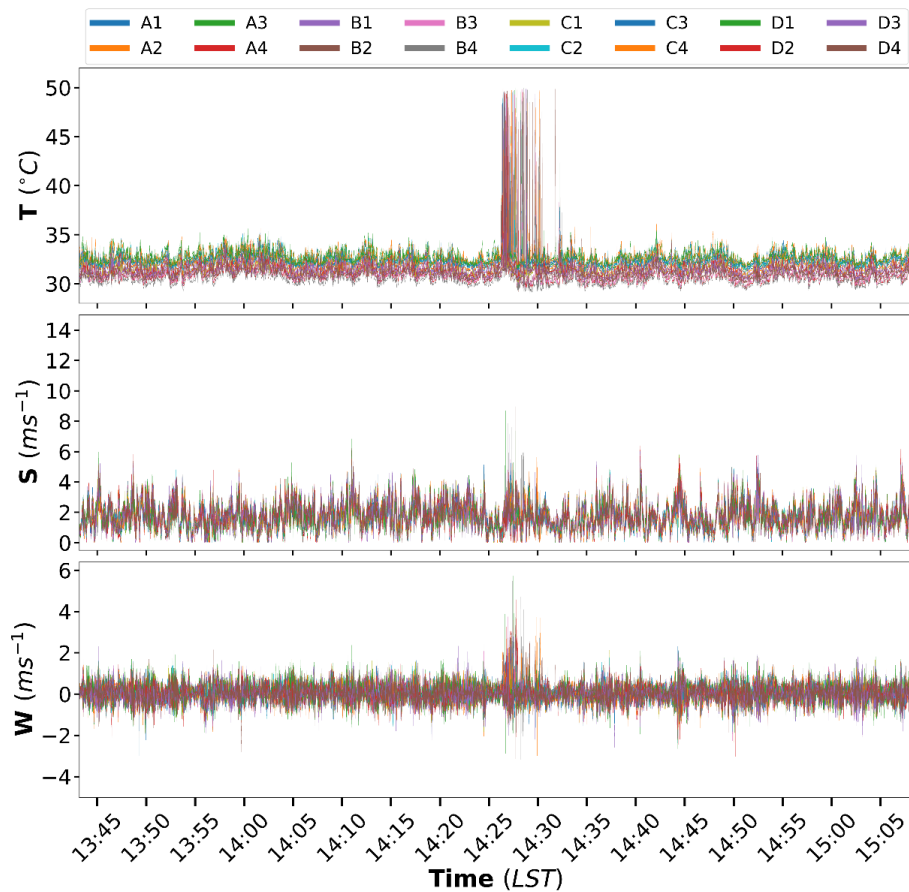
Figure 4. Time series of 10-Hz observations of temperature (T), horizontal wind speed (S) and vertical wind component (w) observed by the 16 sonic anemometers.
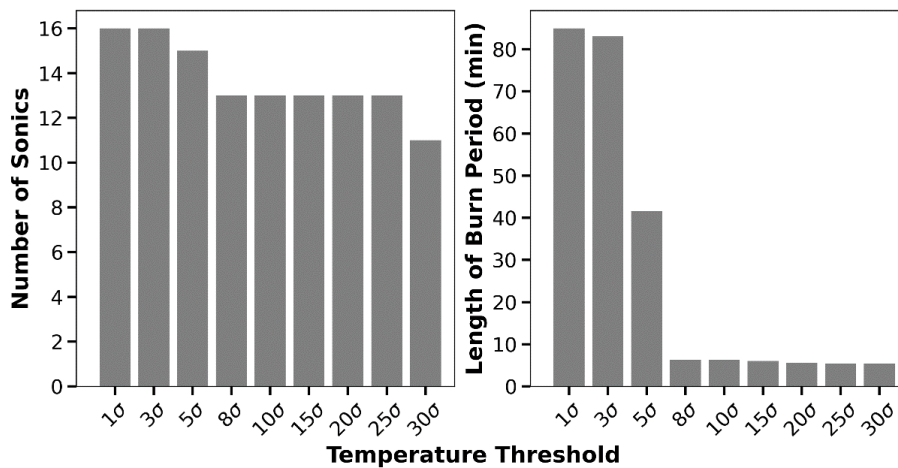
Figure 5. The number of sonic anemometers that recorded temperatures at or above a given threshold value (left) and the length of period over which the threshold was reached or exceeded (right). The symbol σ denotes pre-burn period temperature standard deviation.
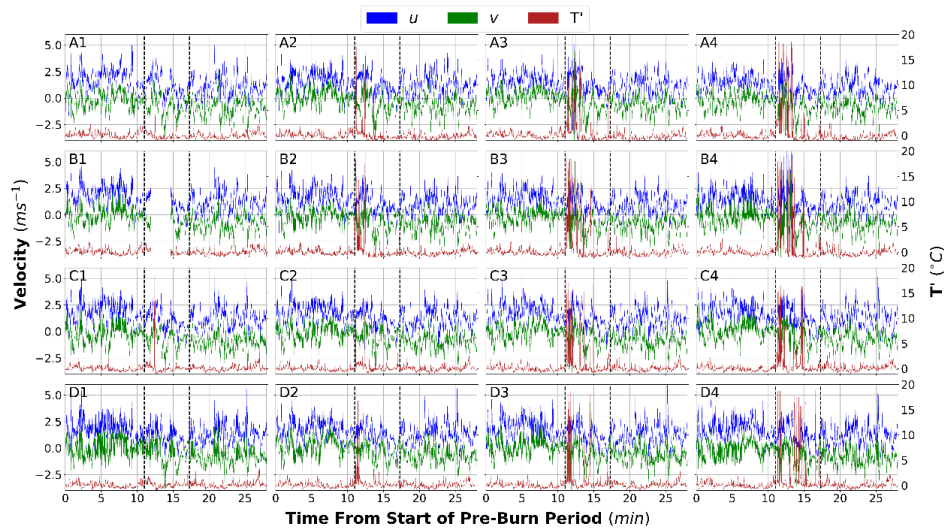
Figure 6. Time series of 10 Hz streamwise (u, blue) and cross-stream (v, green) wind velocity components and temperature perturbations (T', red) recorded by each sonic anemometer at 2.5 m above the ground. The vertical dashed black lines indicate the burn period determined by the first and last occurrence of $T' \geq 8\sigma$. Time is the minutes since the start of the pre-burn period.
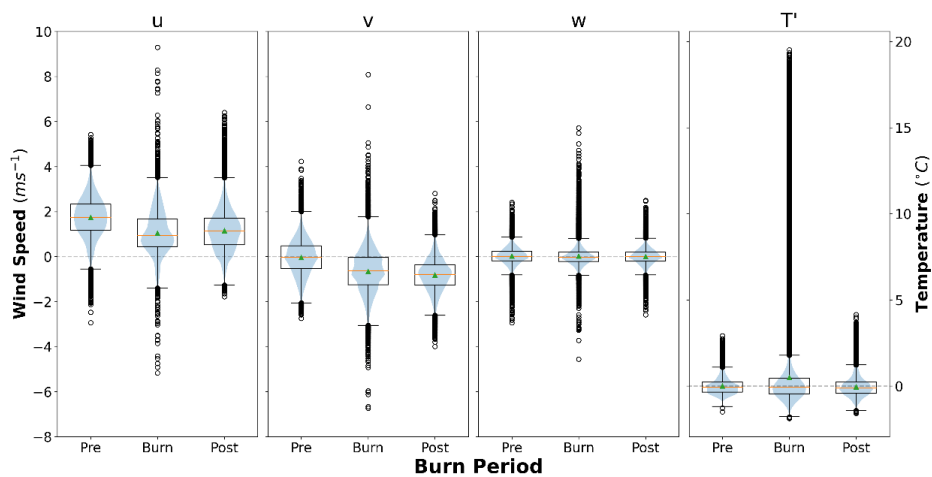
Figure 7. Distributions of 10 Hz streamwise (*u*), cross-stream (*v*), and vertical (*w*) wind velocity components, and temperature perturbations (*T'*) from all 16 sonic anemometers during pre-burn, burn and post-burn periods. The box represents the *25th* and *75th* percentile of the data, with data inside the whiskers representing *99.3%* of the data. The orange line in the boxes is the median value, the green triangle is the mean, and the blue shading is the density of values of the data.
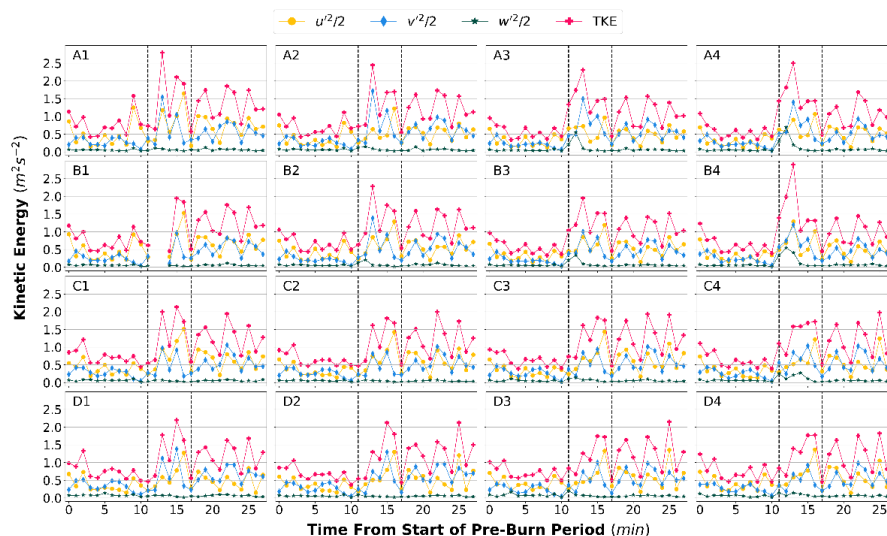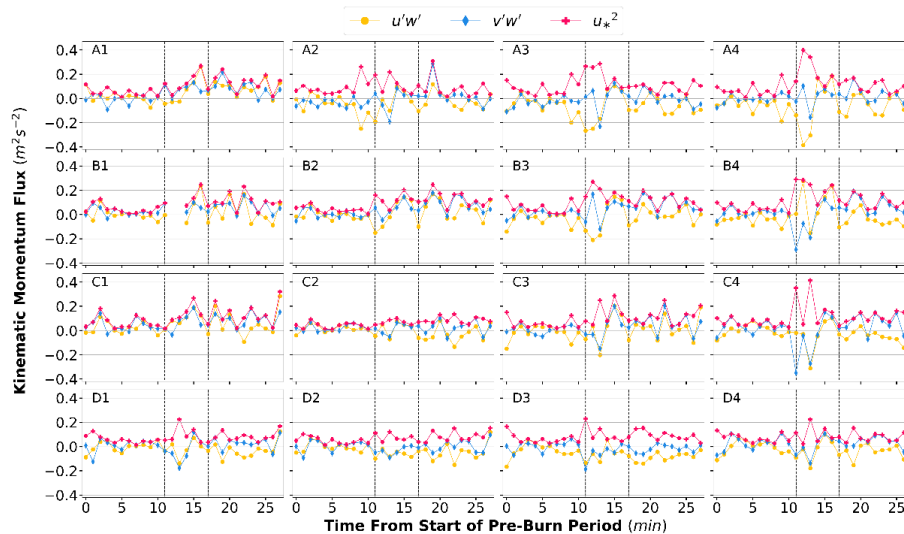
Figure 8. Time series of 1-minute averaged turbulent kinetic energy (*TKE*) (red) for each sonic anemometer and the three components of velocity variance, $u'^2/2$ (yellow), $v'^2/2$ (blue) and $w'^2/2$ (green), that make up the *TKE*. The vertical dashed black lines indicate the burn period determined by the first and last occurrence of $T' \geq 8\sigma$. Time is the minutes since the start of the pre-burn period
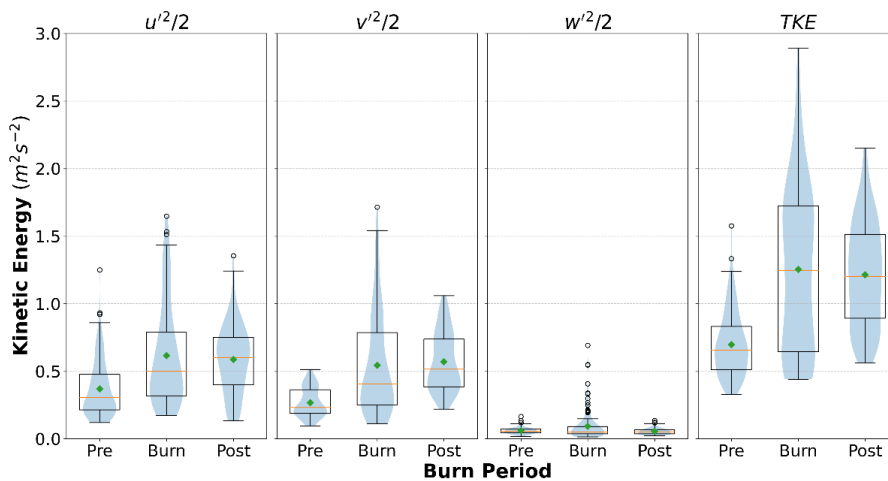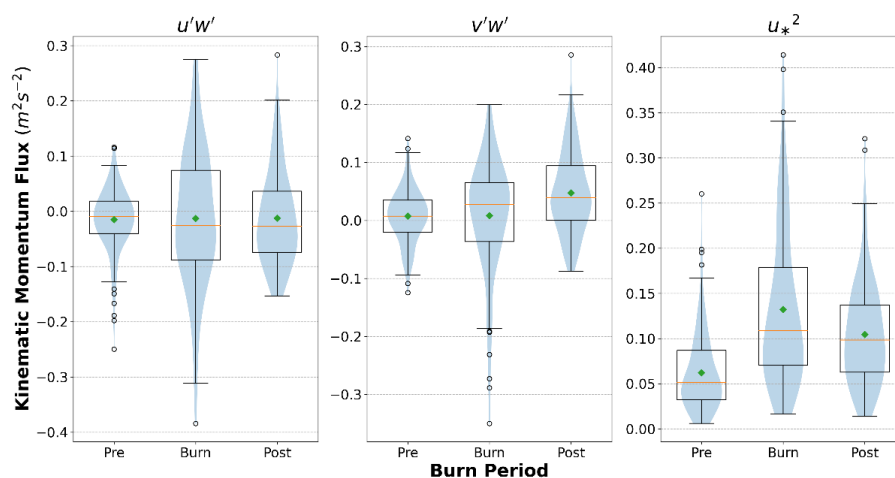
Figure 9. Distributions of turbulent kinetic energy (*TKE*) and the three components of velocity variance (*u'²/2*, *v'²/2* and *w'²/2*) that make up the *TKE* from all 16 sonic anemometers during the pre-burn, burn and post-burn periods. The box represents the 25th and 75th percentile of the data, with data inside the whiskers representing *99.3%* of the data. The orange line in the boxes is the median value, the green triangle is the mean, and the blue shading is the density of values of the data.
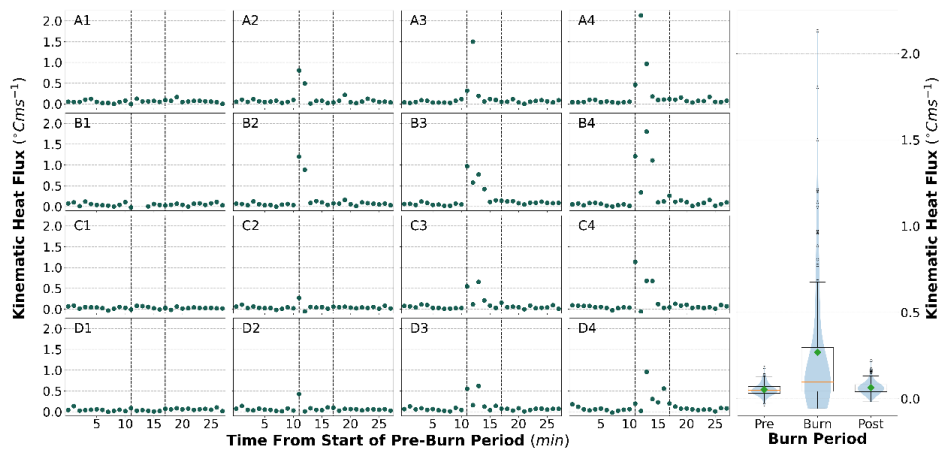
Figure 10. Time series of 1-minute averaged friction velocity squared (u_*^2, pink pluses) and its two components, the streamwise kinematic momentum flux, $\overline{u'w'}$ (yellow circle) and the cross-stream kinematic momentum flux, $\overline{v'w'}$ (blue diamonds), for each of the 16 sonic anemometers. The vertical dashed black lines indicate the burn period determined by the first and last occurrence of $T' \geq 8\sigma$. Time is the minutes since the start of the pre-burn period.

Figure 11. Distributions of friction velocity squared ($u_*{}^2$) and its two components ($\overline{u'w'}$ and $\overline{v'w'}$) from all 16 sonic anemometers during the pre-burn, burn, and post-burn periods. The box represents the 25th and 75th percentile of the data, with data inside the whiskers representing 99.3% of the data. The orange line in the boxes is the median value, the green triangle is the mean, and the blue shading is the density of values of the data.
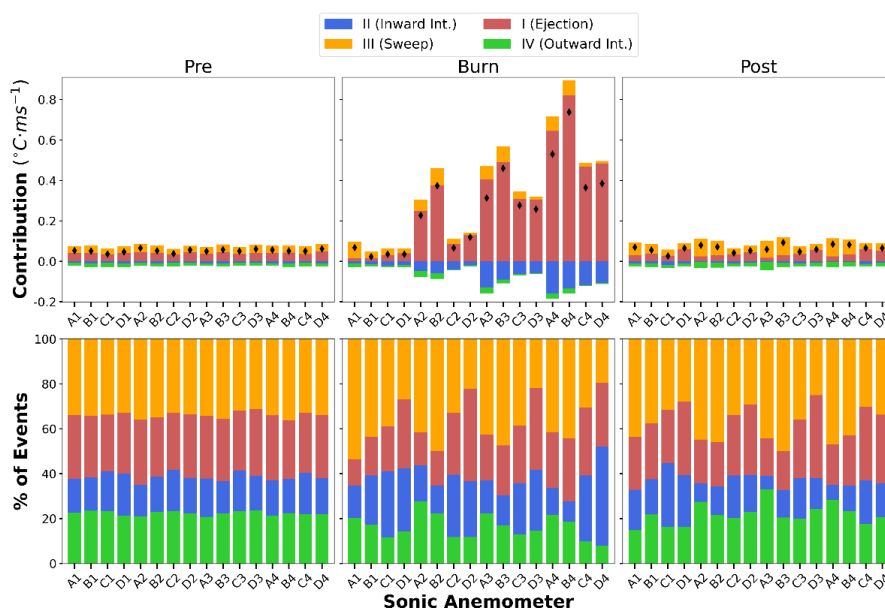
Figure 12. Time series of 1-minute averaged heat flux for each of the 16 sonic anemometers (left) and the distribution of heat fluxes from all 16 sonic anemometers during the pre-burn, burn, and post-burn periods (right). The box represents the 25th and 75th percentile of the data, with data inside the whiskers representing *99.3%* of the data. The orange line in the boxes is the median value, the green triangle is the mean, and the blue shading is the density of values of the data.

Figure 13. Quadrant analysis of the instantaneous vertical kinematic turbulent heat fluxes showing the contributions to the total flux from (top row), and the percent of (bottom row) the four types of events: outward interaction (green), ejection (red), inward interaction (blue), and sweep (orange) for each of the 16 sonic anemometers during the pre-burn, burn, and post-burn periods. The black diamonds in the top row indicate the total heat flux values. The sonic anemometers are arranged from west to east roughly following the fire spread across the burn plot.
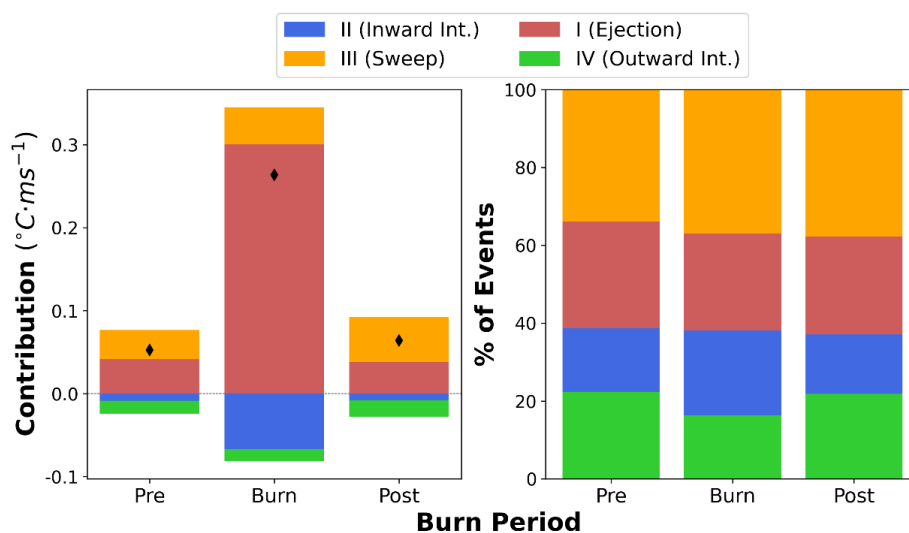
Figure 14. Quadrant analysis of the instantaneous vertical kinematic turbulent heat fluxes showing the contributions to the total flux from (top row), and the percent of (bottom row) the four types of events: outward interaction (green), ejection (red), inward interaction (blue), and sweep (orange) for all 16 sonic anemometers during the pre-burn, burn, and post-burn periods. The black diamonds in the top row indicate the total heat flux values. The sonic anemometers are arranged from west to east roughly following the fire spread across the burn plot.
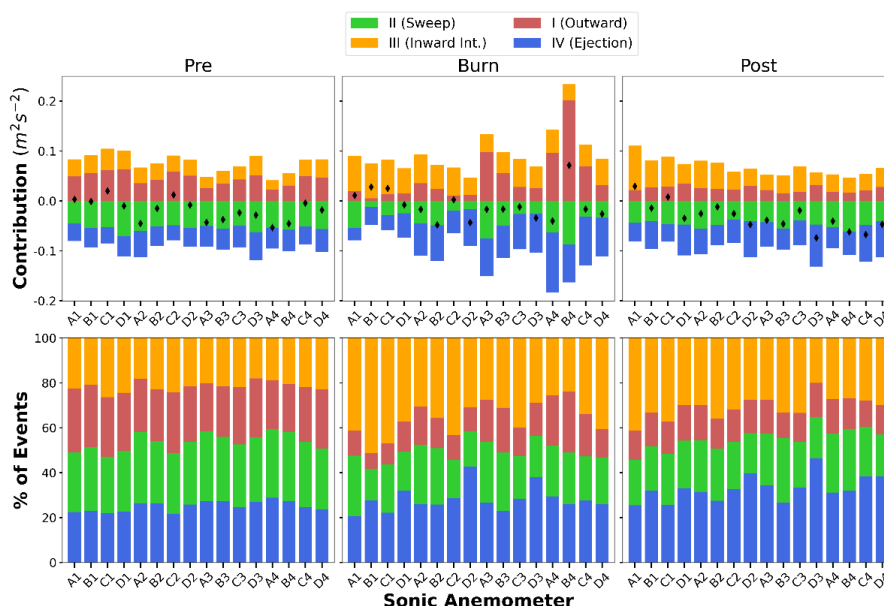
Figure 15. Quadrant analysis of the instantaneous vertical kinematic turbulent fluxes of horizontal momentum showing the contributions to the total flux from (top row), and the percent of (bottom row) the four types of events: outward interaction (red), sweep (green), inward interaction (orange), and ejection (blue) for each of the 16 sonic anemometers during the pre-burn, burn, and post-burn periods. The black diamonds in the top row indicate the total flux values. The sonic anemometers are arranged from west to east roughly following the fire spread across the burn plot.
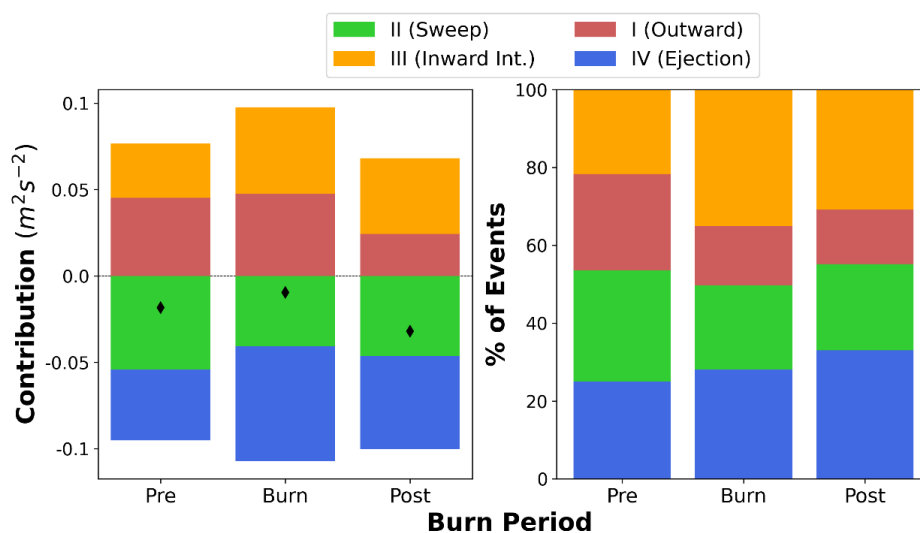
Figure 16. Quadrant analysis of the instantaneous vertical kinematic turbulent fluxes of horizontal momentum showing the contributions to the total flux from (top row), and the percent of (bottom row) the four types of events: outward interaction (red), sweep (green), inward interaction (orange), and ejection (blue) for all 16 sonic anemometers during the pre-burn, burn, and post-burn periods. The black diamonds in the top row indicate the total flux values. The sonic anemometers are arranged from west to east roughly following the fire spread across the burn plot.